2008

Transport properties in nanocrystalline silicon and silicon germanium

Satyalakshmi Saripalli
Iowa State University

Recommended Citation

Saripalli, Satyalakshmi, "Transport properties in nanocrystalline silicon and silicon germanium" (2008). *Graduate Theses and Dissertations*. 10977.
https://lib.dr.iastate.edu/etd/10977

Transport properties in nanocrystalline silicon and silicon germanium

by

Satya Saripalli

A dissertation submitted to the graduate faculty

in partial fulfillment of the requirements for the degree of

DOCTOR OF PHILOSOPHY

Major: Electrical Engineering

Program of Study Committee:
Vikram Dalal, Major Professor
Joseph Shinar
Kristen Constant
Mani Mina
Rana Biswas

Iowa State University

Ames, Iowa

2008

TABLE OF CONTENTS

LIST OF TABLES

LIST OF FIGURES

ACKNOWLEDGEMENTS

I would like to take this opportunity to express my thanks to those who helped me with various aspects of conducting research and the writing of this thesis.

First and foremost, Prof.Vikram Dalal for his guidance, patience and support throughout this research and the writing of this thesis. This thesis would not have materialized but for his insights and words of encouragement that have often inspired me and renewed my hopes for completing my graduate education. I would also like to thank my committee members for their efforts and contributions to this work: Prof.Kristen Constant, Prof.Mani Mina, Prof.Rana Biswas and Prof.Joseph Shinar.

I would like to thank Max Noack for various discussions and helpful suggestions during various experiments. Also I am grateful to my fellow ex-graduate students at MRC: Dr.Sharma, Dr.Panda, Dr.Wang, Dr.Muthukrishnan, Dr.Ghosh, Dr.Jaju, Dan Stieler , Atul Madhavan and Edward Li. I am grateful to Jane Woline for her help with all the paper work during my PhD and for all her cakes and barbecues.

I would also like to acknowledge financial support provided by NSF which partly supported my research.

ABSTRACT

Nanocrystalline(nc-) Si:H and (Si,Ge):H films are important electronic and optical materials. They consist of crystallite grains surrounded by amorphous tissues. To successfully apply these materials for solar cell applications we need to understand their fabrication procedures and develop ways to characterize the material. Transport properties determine whether the generated photons in the device effectively reach the terminal and contribute to the output current. While there are several reports in literature about growth and the carrier transport mechanism in nc-Si, nc-SiGe is a fairly new material. Motivation to study nc-SiGe comes from its lower bandgap which makes it an alternative material for lower cell in tandem devices.

This thesis deals with measurement of fundamental transport properties in these materials like minority carrier lifetime and diffusion length. While there have been previous reports of diffusion length, lifetime was never measured before in nc-Si or nc-(Si,Ge). We adopt the reverse recovery method to calculate lifetime in device type structures. The typical values of lifetime in nc-Si and nc-SiGe were found to be in the range of 300-600ns and 150-250ns respectively. Systematic measurement of lifetimes and defect densities in the same solar cell devices enabled us to prove that Shockley Read-Hall (SRH) recombination holds true in these nanocrystalline materials. With respect to temperature we found that the lifetime follows a U shape, with a decreasing trend till a certain temperature and increasing thereafter. Both the effects could be explained by understanding the actual recombination process. We could get an estimate of the trap locations from lifetime versus temperature data. By examining the reverse recovery waveforms in different types of device structures, we deduced that this method is appropriate when the carrier transport is diffusion dominated.

Lifetime and diffusion length were measured in p^+-n-n^+ devices where the base layer(n) was

either nc-Si or nc-SiGe fabricated using VHF plasma deposition, at a frequency of 46MHz using mixtures of SiH_4 and GeH_4 with H_2. From Raman spectroscopy it was observed that nc-SiGe requires significantly higher Hydrogen dilution ratios compared to nc-Si. Graded TMB doping was used to enhance carrier collection in the base layer. Defect densities were measured using capacitance spectroscopy. In SiGe devices it was observed that extreme care has to be taken at the $p^+ - n$ and $n - n^+$ interfaces to ensure efficient carrier collection. Even though the actual process of grain growth is still unclear in nc-SiGe, from the lifetime versus defect density data, we do conclude that the carrier transport is primarily controlled by recombination at grain boundaries.

CHAPTER 1. ABOUT THIS RESEARCH

1.1 Introduction

Much attention has been devoted in the past decade towards the problem of increasing greenhouse gases in the outer atmosphere. The atmospheric concentration of CO_2 increased from 280 to 380 (in parts per million level by volume) from 1750 to 2003 [1]. The same was recognized at an international level in Kyoto protocol in 1997 to avoid any devastating effects of global warming [2]. Also the oil prices have increased from \$85(an year back) to \$135(today) and are expected to shoot to \$185 by the end of 2008 [3].

Photovoltaic(PV) energy is one of the key clean and green energy resources for the simple reason that it does not consume fossil fuels and thus makes it easier to achieve balance of ecological cycles of the biosystems on the earth. Other alternatives like Wind and tidal powers are very location dependent and are severely limited. The single largest barrier to the adoption of solar energy is the cost issue, which has led to the interest in thin film technology.

Initially, solar cells with high efficiency have been made from crystalline silicon. The material itself and the processing were expensive making this unviable for large scale production. This technology involves several steps like silicon purification, crystal growth and wafering, cell processing, and cell encapsulation. Among these steps the cost of the wafers itself makes up to 50% of the cost. But the technology is well understood with the average module level efficiency being 15-20% and provides a reliability of >10years. c-Si based solar cells have captured 93% of the PV market as of 2003 [4].

Since early 80's extensive research had been performed to *deposit* silicon instead of using crystalline silicon wafers. Other than the enormous cost relief, we also now have the freedom of working with non-circular cells which might be better while installing bigger modules and to easily manufacture large area and flexible structures. A quick look at the reduction in cost of PV installations through the years will help us realize the real drive behind the research in thin film technology. The prices for high power band (>70 Watts) solar modules has dropped from around \$27/Wp in 1982 to around \$4/Wp 2006 [5] and is expected soon to reach <1/Wp.

Amorphous Silicon (a-Si:H) is relatively a matured thin film technology with highest efficiencies of solar cells reported (with a-Si:H as the i-layers) being in the range of 9-10%. Besides offering several advantages like high absorption coefficient [6] and ease of fabrication at low temperature, this material suffers from light induced degradation and low deposition rates. On the other hand we have poly-crystalline silicon which is significantly expensive to manufacture compared to amorphous silicon but has the ability to give stable and high efficient devices because of its crystalline structures. This gave rise to the interest in a material like nanocrystalline silicon(nc-Si) wherein we try to deposit crystallites of silicon using the low cost methods like PECVD. So by carefully adjusting the deposition parameters we can achieve good crystallinity at a low temperature depositions and do not need any expensive laser equipment like the case of poly-Si. We now discuss more about the material: nc-Si.

1.2 About the material

The nomenclature of different types of silicon deposited using thin film technology are based on the structure, mainly the grain size. On one end of the spectrum we have polycrystalline silicon which consists of grain sizes of the order of 100's of microns. We also have *microcrystalline*(μc) and *nanocrystalline*(nc)- silicon, though μc-Si and nc-Si are used interchangeably in literature, the former has a grain size of a few microns and the latter has grains with typical sizes of 10-100nm.

Basically nc-Si consist small grains(10nm) surrounded by a-Si:H tissues and significant bonded hydrogen with the atomic hydrogen at 5% level compared to 9-10% for a-Si:H. The hydrogen bonds play the role of passivating the dangling bonds at grain boundaries and the a-Si tissues fill the region between the grains which can span a region of a few nm in size. Therefore ensuring that the carriers are able to move from one grain to the next without recombining at the grain boundaries or in the a-Si regions is *the* most important condition that needs to be satisfied before we can expect good transport of carriers in nc-Si. In fact, it is because of the well passivated grain boundaries in nc-Si that efficiencies in nc-Si and poly-Si are comparable (10%) inspite of the drastic difference in their grain sizes.

The key topics that need to be studied to obtain maximum efficiency achievable from nc-Si material are [7, 8, 9]

- Ability to deposit larger crystallites at low temperatures
- Role of grain boundaries in carrier transport
- Effect of hydrogen incorporated in the material

The carrier transport is quantized in terms of three main properties diffusion length, carrier lifetime and mobility. The first two of these are directly related to the minority carrier recombination, which has been postulated to take place mainly at the large grain boundaries.

1.3 Objective

The importance of the carrier transport properties in solar cells becomes evident if one examines the requirements for higher currents in a solar cell. The two main factors are absorption of more photons and collection of the generated electron hole pairs as shown in Figure 1.1. While the former depends more on bandgap of the materials, the latter depends on the quality of the material used in the base layer of the device. Too many defects result in carrier loss, which means several e-h pairs generated actually recombine before they reach the positive and negative electrodes of the cell.

While several research efforts have been devoted to study the effect of various deposition parameters on the efficiency of a device, it is important to measure the fundamental transport properties in device structures to exactly point out the loss mechanism. Other than the normal I-V and quantum efficiency data, we need methods to calculate these properties. We did not find adequate methods to quantitatively measure the lifetime of minority carriers in the

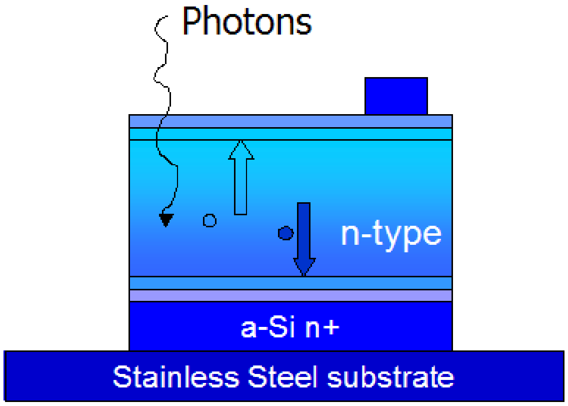

Figure 1.1 Schematic diagram showing photon absorption and carrier collection in solar cell

nc-Si material in literature. Also, it will be explained in later chapters that, the carrier transport is anisotropic in nc-Si and hence the experimental techniques to measure these transport properties should measure the properties in the correct direction (transverse vs longitudinal).

The most important part of this thesis is the development and characterization of lifetime measurement technique using reverse recovery method. This method has been selected because of its simplicity in constructing the experimental setup and also the transport takes place along the grains which is a important for a nc-Si PV device. The limitations and applicability of this methods have been carefully studied. Also was measured diffusion length using quantum efficiency, which was already proved to work in nc-Si material in literature [10]. To verify that SRH recombination model holds true, lifetime and diffusion length had to be measured as a function of defect densities. The effect of temperature on lifetime was studied which revealed important information about the trap location.

The solar cells devices required for these experiments were deposited using VHF PECVD method with nc-Si and nc-SiGe as the i-layers in the p-i-n devices. Significant number of experiments were devoted to study nc-SiGe, like effect of deposition parameters on the film quality using Raman and XRD spectroscopies, and the device properties themselves like short circuit current and fill factor.

CHAPTER 2. REVIEW OF LITERATURE

In this chapter we shall review the previous work done by various research groups in the field of microcrystalline and nanocrystalline silicon, how the fabrication methods and experiments measuring carrier transport and other electrical properties have developed through the years. Since considerable experiments in this project were also done in nanocrystalline silicon germanium, some of the previous work related to nc-(Si,Ge) will also be covered. Both these materials are important solar cells[11, 12, 13], sensors[14, 15] and thin film transistor(TFT)s[16, 17]. Also shall discussed are the various reports of minority carrier lifetime measurements done in crystalline and microcrystalline silicon and the original work by Lax et.al and Kingston et.al in formulating the reverse recovery method.

2.1 Hydrogenated Nanocrystalline Silicon (nc-Si:H)

2.1.1 Why nc-Si?

Nc-Si:H offers several advantages compared to a-Si:H or other technologies which makes it an ideal material for the future generation PV devices, the important of these are listed below

- Nc-Si:H does not show the light induced degradation which has been the limiting the factor for expansion of a-Si:H
- As compared to a-Si:H, the mobilities are higher, since we have grain structures in nc-Si:H. This means that nc-Si:H can potentially give rise to more current densities
- The presence of the small grains also provides the capability of achieving significantly higher minority carrier diffusion lengths and recombination lifetimes than a-Si:H.

- The smaller band gap than a-Si:H makes it an ideal candidate for the bottom cell in a tandem device.
- It also satisfies the important material requirements for PV application like low cost and low temperature deposition (<400C). The most common method of depositing nc-Si:H is by PECVD using SiH_4 and H_2 gases.
- Because of the absence of band tails efficient doping of nc-Si:H can be achieved and hence this material can be used as the ohmic contact in solar cell devices and in TFTs.

History of μc-Si:H

Veprek and Marecek in 1968[18]reported the deposition of μc-Si:H for the first time using chemical transport method. Usui et.al showed that doped μc-Si:H can be deposited using high power inductive glow discharge of Silane[19]. Since the early days it was observed that as deposited μc-Si:H tends to be n-type and is always defective which turned out to be a hindering factor for the incorporation of μc-Si:H as the i-layer in n-i-p or p-i-n solar cells[20]. Other than the lack of understanding of material properties and the ways to deposit device quality μc-Si:H, low deposition rates of $1\AA s^{-1}$[21] was another hindering factor for the research in this field.

Neuchatel's group was one of the first to report solar cells made entirely from μc-Si:H. They showed that compensated μc-Si:H can be deposited by incorporation of ppm levels of diborane[22]. The electrical characteristics of solar cells indicated that the carrier transport was happening in the crystalline phase of the material. Alternative way to ensure mid gap character of μc-Si:H is by the silane gas purifier technique[23].

After 40 years of research efforts on this thin film semiconductor we have theories which can explain, partially, the carrier transport over the dimensions of the order of 1μm which clearly cannot suffice for thicker solar cells or TFTs, where the transport is parallel to the substrate and extends to the dimensions of 10-100μm.

2.1.2 Material Growth

2.1.2.1 Deposition Method of μc-Si:H

The predominant method used for deposition and amorphous and microcrystalline semiconductors is a PECVD technique where in plasma is electrically excited in with an applied RF voltage whose frequency was fixed at 13.56MHz for a long time. It was observed that higher deposition rates could be achieved by increasing the frequencies to the range of 100MHz, termed as very-high-Frequency(VHF)[24, 25, 26]. In this section we first briefly review the theory behind VHF PECVD, its advantages and then present the specific results from literature obtained in nc-Si material.

Very High Frequency (VHF) PECVD

Figure2.1, shows the deposition rate of μc-Si:H versus plasma excitation frequency. The data is repeated at three different pressures. We see a monotonous increase of deposition rate by 4 times from 13.56MHz to 70MHz. Also, the deposition rate slightly increases with pressure. Similar trend was found in depositions of a-Si:H, and it was also checked that the film quality did not degrade at higher deposition rates by Urbach energy and defect density measurement and no stress was seen in the films. In case of μc-Si:H, Raman and TEM studies showed that no degradation of crystallinity was seen at higher frequencies. Also the grain size from XRD measurement increased from 13nm at 27MHz to 32nm at 120MHz. In this span of grain sizes Hall mobility almost doubles from 0.8cm^2/Vs to 1.6cm^2/Vs. Finger et al, explained these results based on the etching growth model of μc-Si:H. This model assumes that growth of μc-Si:H is a result of the balance between two phenomena: etching of the amorphous phase and the grains and the growth of the actual crystalline material. Tsai et al and several other groups reported that it is difficult to obtain bigger grains at higher deposition rates wherein the crystals do not have enough time to reconstruct at grain boundaries to form bigger grains. So by ensuring preferential etching of the amorphous silicon between the grains and also some of the crystalline nuclei we can expect to obtain larger grains.

Satake et al showed from simulations that VHF power is positively correlated with plasma potential and electron density. Though higher electron density is useful for higher deposition

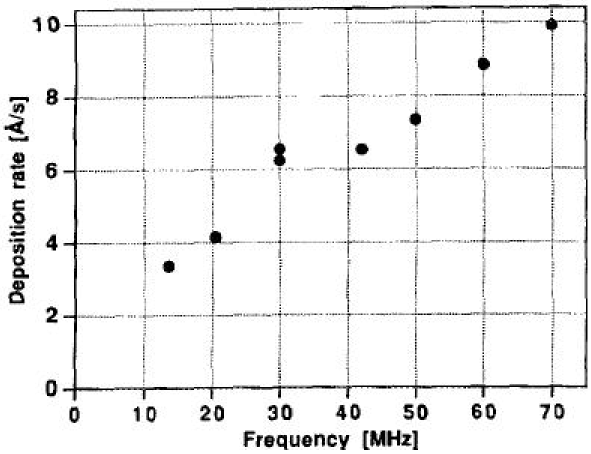

Figure 2.1 Deposition rate versus RF frequency in a RFPECVD system, at a constant power of 5W for an a-Si film [27]

rates, higher potential implies ion damage which can disrupt the crystal growth[28]. On the other hand the excitation frequency has he right kind of relation: it is positively correlated with electron density but negatively with plasma potential. The same behavior was observed experimentally by Perret in [29], shown in Figure2.2. The high frequency plasma offers the advantage of achieving higher ion fluxes at lower energies which are required to attain good crystallinity in microcrystalline silicon. One limitation might be the case when higher energies are also needed for enhanced etching, which points out the origin dual frequency plasma processes. This gives us independent control of ion flux and energy.

The problem of powder formation is greatly reduced in VHF plasma partly because of the lower sheath potentials, which help in lesser accumulation of powder. Howling et al[27] reported that at 70MHz discharge only a thin disc of powder was observed at the plasma/sheath boundary, while the observed width and intensity were much higher at lower frequencies[30]. The lower plasma potential at these higher frquencies implies that the excitation frequency can be increased beyond 70MHz before the any detrimental effects of ion bombardment can be seen.

It was also observed from OES studies that the intensity of SiH* and H_2^* lines increased by factors of 2.5 and 3.8 respectively. Even though SiH* is not directly related to the growth

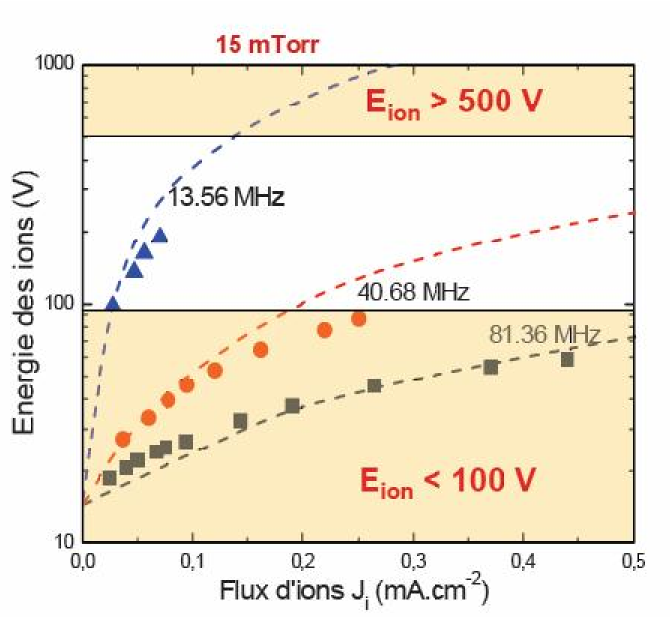

Figure 2.2 Ion energy vs ion flux, for three different frequencies in an argon plasma at 15 mTorr[29]

mechanism its correlation with higher deposition rates indicated that in VHF plasma we have better dissociation of gases and hence more radicals are available which can enhance growth rates[31, 90]. We are effectively better utilizing the gases in this case compared to low frequency plasma.

Growth Mechanisms

The fundamental mechanism on which the various growth models are based is that the process is primarily governed by dissociation of silane into silyl radicals and their adsorption onto the film surface. The process further repeats by creation of fresh vacancies for these radicals by abstraction of H from surface. There are three main models in literatures which explain this process in three fundamentally different models, out of which surface diffusion models is the one more commonly accepted.

1.*Surface diffusion model*

This model, proposed by Matsuda et.al in 1983 explains the growth of nc-Si based on the surface diffusivity of the growth radicals. We need sufficient flux density of atomic hydrogen to obtain full coverage by bonded hydrogen to enhance surface diffusion of film precursors like

SiH_3. Any heat released by hydrogen recombination reactions on the film surface can also help. They reported that good crystallinity is obtained under high hydrogen dilution and low power densities. Also at a given hydrogen dilution, as we increase temperature surface diffusivity increases giving rise to better crystallinity but after a certain point dangling bonds created by thermal dissociation start to dominate above 400C and crystallinity degrades [33, 36]. Similar models have also been proposed in [34, 35]

2.*Etching model*

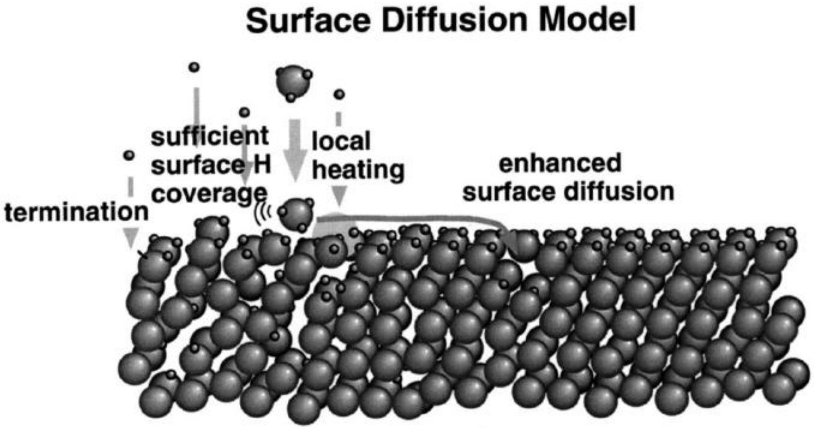

Figure 2.3 Schematic diagram explaining the surface diffusion model of nc-Si film growth [33]

This is a simple model which assumes that the flux of Hydrogen ions preferentially etches weaker Si-Si bonds (like the bonds in a-Si phase) on the film surface while not disturbing the stronger crystalline Si-Si bonds [37]. There is a continuous balance between etching and growth. Thus, unless the energy of H ions is too high as H dilution increases growth rate decreases. But it was observed from the studies of growth rate versus flu density of film precursors, that removal process of weakly bonded Si atoms is not necessary for the formation process of nc-Si.

3.*Chemical annealing model*

It has been observed that by exposing a thin layer of a-Si film to H_2 plasma treatment, the film can actually be crystallized and by repeating that process several times we can obtain a nc-Si film [**?**, 39]. Also it was observed that the hydrogen plasma does not reduce the thickness which contradicts the etching model. Hence it was proposed that the H ions permeate into the film (within the growth zone) and crystallizes the a-Si phase through the formation of flexible network.

Another interesting insight provided by Dalal et.al [40] is that the growth of a-Si is primarily controlled by removal of adjacent H atoms from adjacent SiH3 radicals. This can obtained through H ion bombardment or inert gas ions. While H ions can participate in surface and subsurface reactions, inert ions can only help in surface reactions. The energy of H ions need to high enough(2-3eV) to successfully react with the weakly bonded Si-H bonds. Also, inert ions like Ar can dissociate SiH4 more effectively than H and hence result in higher deposition rates. Therefore it is beneficial to have both H and Ar ions for better a-Si film quality. Although this model was explained in context of a-Si, it can be useful in understanding growth of nc-Si.

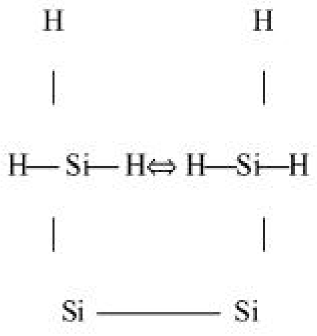

Figure 2.4 Schematic diagram showing the abstraction of adjacent H atoms required for void free film growth [40]

2.1.3 Material properties

Optical properties

Optical absorption is an important character for PV materials. Figure 2.5 shows the absorption coefficients of μc-Si:H compared to a-Si:H and crystalline silicon. The higher α value seen in μc-Si:H as compared to c-Si is proved to occur due to the light scattering effect because of the inherent surface roughness associated with the growth of μc-Si:H (will be explained later). The fact that sub bandgap(below 1.1eV) absorption is still low (less than 1) in μc-Si:H indicates that defect densities are still very low [41].

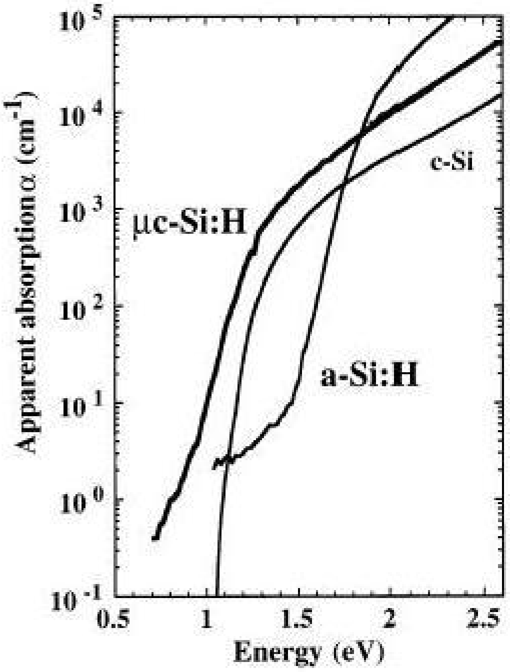

Figure 2.5 Effective absorption coefficient of μc-Si:H [41]

Structural properties

Growth of μc-Si:H can be divided into three stages: incubation layer, transition to fully microcrystalline growth and further development of the columnar grain aggregates. The macroscopic transport properties will depend on the percentage of crystalline fraction, quality of the film within those crystalline grains and the amorphous phase. So measuring a global transport property like diffusion length or minority carrier lifetime by itself may not render much useful information. We need to know how exactly the geometry of the film changes as the grains grow.

2.1.3.1 Growth of μc-Si:H

Figure 2.6 shows the AFM images of a series of μc-Si:H films with different thicknesses. We can clearly see how the approximately conical crystal grains collide and create almost straight boundaries. Figure 2.7 shows cross sectional TEM from a different publication explaining the same phenomena. Kocka et.al showed that the straight line boundaries proceed until the whole sample plane is covered by grains forming a so called *Voronoi tessellation.*

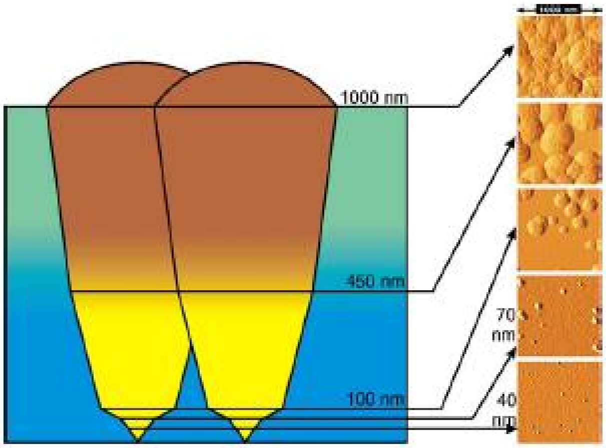

Figure 2.6 Evolution of grains and the corresponding AFM topography views measured at various thicknesses [44]

Figure 2.7 shows the cross sectional TEMs for two μc-Si:H films deposited at different hydrogen dilution ratios, defined by $R = [H_2]/[SiH_4]$. A comparison of these TEMs indicates clearly that higher hydrogen dilution leads to higher nucleation density(N_d). Also the film with higher R has thinner d_{nuclei} (initial a-Si:H thickness) and thinner $d_{contact}$ (height at which the grains coalesce). The thinner d_{nuclei} indicated that the structural changes required to occur in the initial a-Si:H layer occur easily at higher R. For a fixed R, it was observed that d_{nuclei} remained fairly constant with the substrate even though the inter nuclear distance was as high as $500\mathring{A}$ [42].

Also studies of surface roughness from in-situ spectroscopic ellipsometry(SE) showed that r.m.s surface roughness is mainly controlled by N_d since the surface roughness increases with the growth of grains until the whole surface is covered by μc-Si:H. The enhanced surface roughness during the growth of μc-Si:H, it is estimated that growth rate of μc-Si:H is 15% more than a-Si:H.

2.1.3.2 Analysis on Grain geometry

- Fejfar et al. [43], performed simulation using Voronoi network geometry, taking the nucleation density and apex angle as the only parameters [43]. Their studies showed that

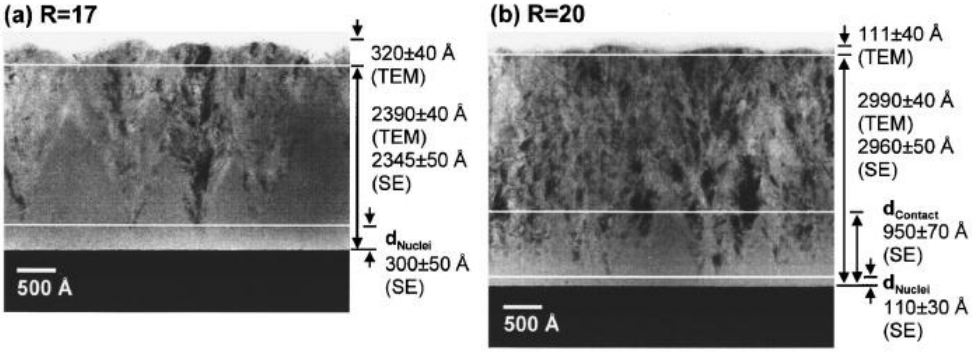

Figure 2.7 Cross sectional TEMs for μc-Si:H films with different hydrogen dilution ratios (a)R=17 and (b)R=20. Comparison of d_{nuclei} and $d_{contact}$ obtained from SE measurements are shown

around the crystalline grain the film is actually void of the amorphous phase over a certain distance as shown in Figure 2.8. This occurs because of the capture of the radicals by the fast growing crystal from the surrounding regions. This led to estimation of diffusion length of the radicals to be 60nm. Figure 2.6 shows how the apex angle changes as the grain evolves. It goes to peak and then decreases back. This means the columnar structures grow in two different stages [18]: expansion and elongation stage.

- While *Voronoi network* explains the grain growth, its dual:*Delaunay triangulation* explains that the grain nuclei are connected with a minimum total length of connection. While analyzing the carrier transport parallel to the substrate, we can understand how the parallel conductance changes as the grains grow. Before the all the grains collide, the current passes through the nearest neighbor since we have longer amorphous tissues between grains in other directions. If all the grains touch each other, we can follow the standard theory and the expect that current is limited by the grain boundaries and is hence inversely proportional to the area of the boundary. Not many experimental results have been performed in this direction, note that this theory is largely borrowed from the way transport is understood in ceramic multi crystals.

- If one is analyzing the transport perpendicular to the substrate, we do not have any

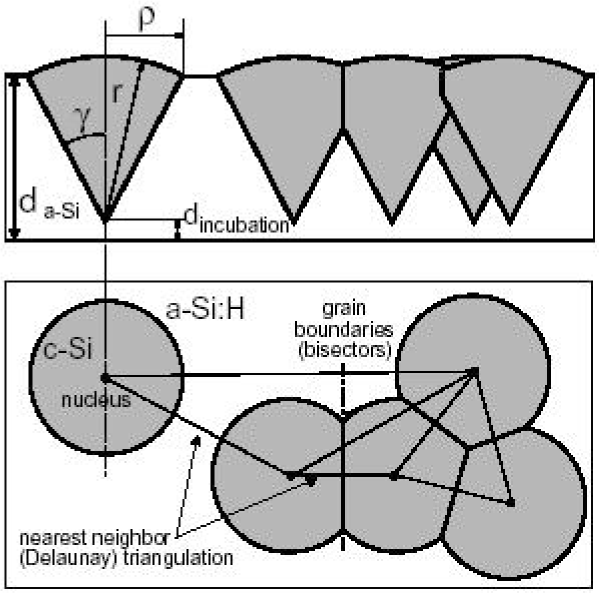

Figure 2.8 Geometry of the μc-Si:H structure model based on the *Voronoi* network model: cross-sectional and top views [43]

significantly new results from this theory. But numerical simulations have been reported by solving the electrostatics of the grain, result shown in Figure 2.9. The simulated example is the vertical voltage drop across a μc-Si:H film. We can see a huge field concentration at the grain tip and the current density also reaches a maximum here indicating that in a sandwich structure we could have even higher field concentrations.

- It was also proposed that the conventional way of treating light scattering in μc-Si:H based on Fresnel formulae may not be valid for higher grain size (100nm to 1μm) [43], since the wavelengths in visible spectrum become comparable to these dimensions. It was also shown that using elementary geometric optics light always gets refracted close to the surface normal. Whichever wavelengths transmit through the μc-Si:H material and get focused at a point close to the nuclei might give rise to some secondary effects due to their back reflection. More research is in progress in understanding these effects better

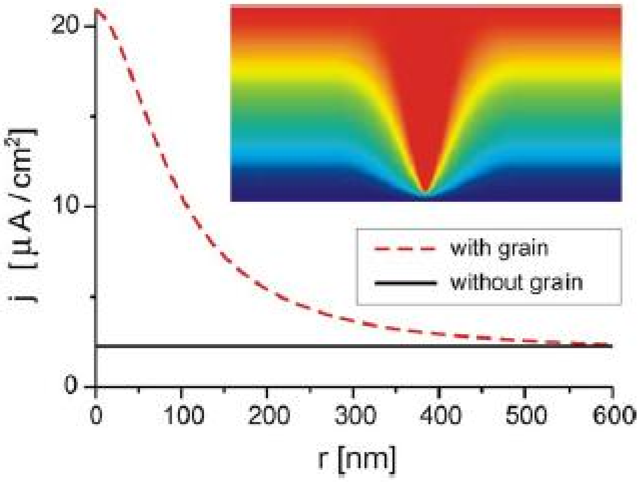

Figure 2.9 Concentration of electric field and current towards the grain tip [43]

2.1.4 Carrier Transport

It has been proposed [44] that the large grains in μc-Si:H are actually composed of smaller grains, with a density of $10^{18} cm^{-3}$. Since the typical defects are of the order of $10^{16} cm^{-3}$, these smaller grains and their boundaries are defect free. Figure2.10[44] shows the plot of conductivity pre-factor, σ_0 and activation energy, E_a versus thickness and crystalline fraction. We can see that with increasing crystallinity E_a decreases because of the upward shift of E_F. The dramatic drop of σ_0 with increasing thickness or equivalently, formation of grain aggregates confirms the common assumption that most of the defects and impurities like O,N,C and H-aggregates to the grain boundaries formed by the a-Si:H tissue at the grain boundaries give rise to a potential barrier.

2.2 Hydrogenated Microcrystalline silicon germanium μc-(Si,Ge):H

2.2.1 Motivation to study μc-(Si,Ge):H

Successful implementation of a-Si:H/μc-Si:H based tandem junction solar cells has been reported[46], where a-Si:H absorbs short wavelengths and μc-Si:H absorbs red to infrared lights that penetrate through the top a-Si:H cell. Thus using a thicker thicker μc-Si:H layer

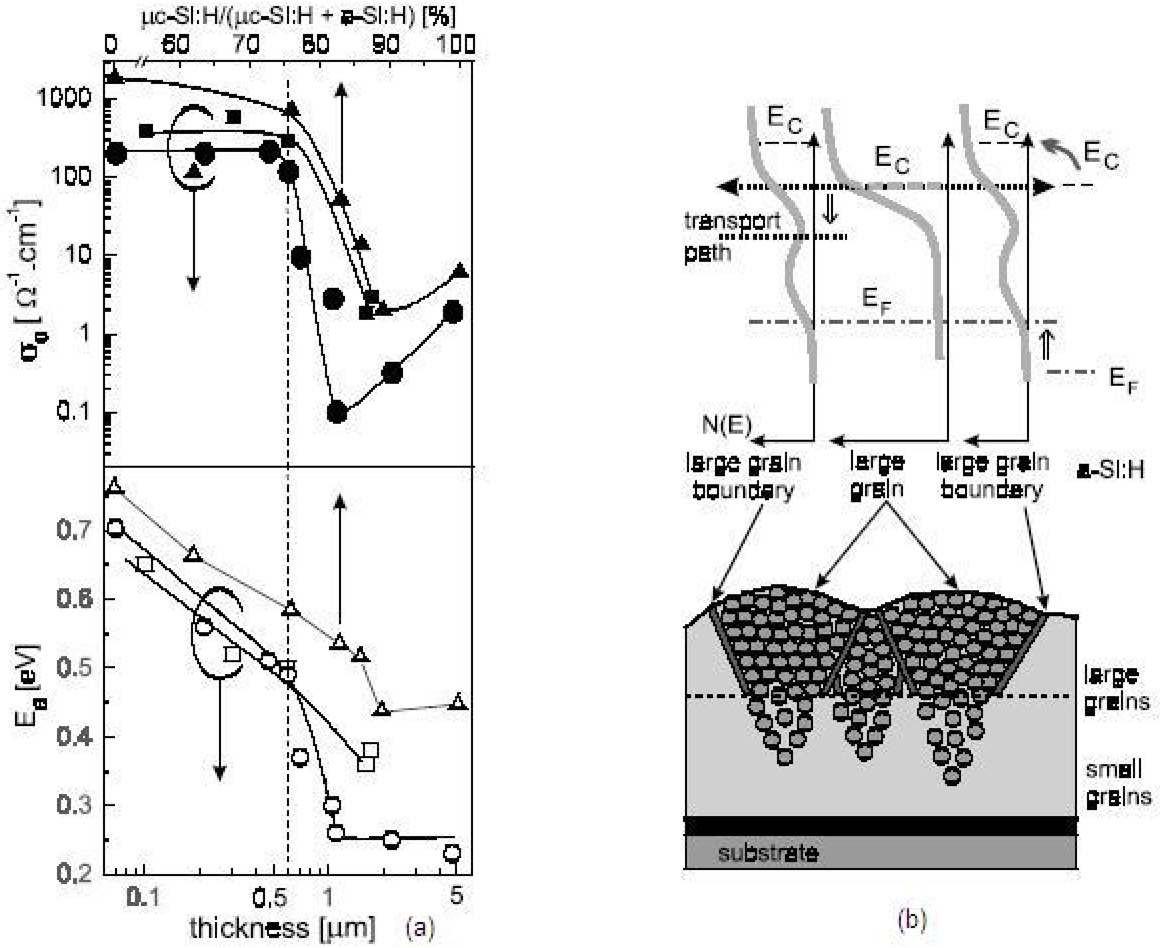

Figure 2.10 (a)conductivity prefactor σ_0 and activation energy, E_a plotted for 3% and 4.5% silane dilution thickness series. Top horizontal axis shows the variation with μc portion (b) Schematic picture of μc-Si structure and the density of states at various places[44]

increases infrared absorption but degrades carrier collection. Hence we need to develop a stronger infrared absorber to improve the efficiencies of solar cells further. Hydrogenated micro(or nano)crystalline silicon germanium (μc-(Si,Ge):H) is the appropriate material in this regard.Also μc-(Si,Ge):H has other applications like TFTs wherein it has the attractive properties like variable bandgap (important in CMOS transistor gates)[47], higher mobility, higher electrical activation energy for dopants in SOI technology[48]. Figure2.11 shows the absorption spectra of μc-$Si_{1-x}Ge_x$ for various relative compositions of Si and Ge. It shows a systematic red shift as the Ge content increases. In the range of 1.5eV to 2.5eV and for x >0.5 the absorption is uniformly 1 order more than μc-Si:H which means theoretically this material is capable of achieving higher current densities than μc-Si:H.

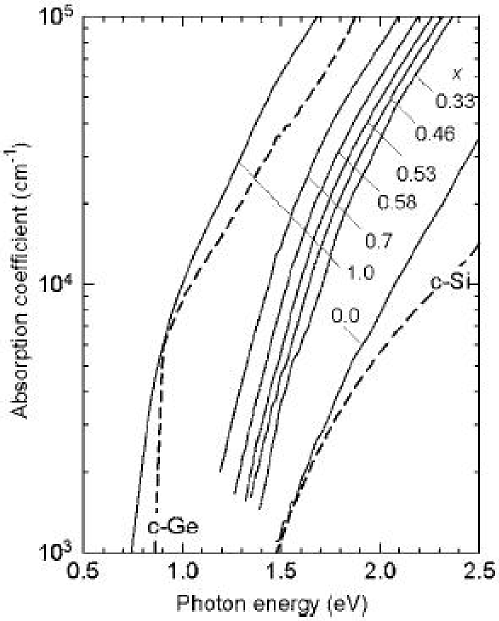

Figure 2.11 Absorption spectra of $\mu c - Si_{1-x}Ge_x$:H for various compositions compared with c-Si and c-Ge[49]

2.2.2 Previous work

2.2.2.1 Material Study

1. Matsui et.al[49] has reported several results on electrical properties' study and application of μc-(Si,Ge):H in solar cell device structures. Figure2.12[49] shows the measured electrical properties of μc-(Si,Ge):H films for various Ge fractions. The value x=0.75 seems to be an interesting point, at which mobility reaches a maximum value of $9cm^2V^{-1}s^{-1}$ and the film changes from n-type to p-type around this fraction. This is in contradiction with the other reports which show that the mobility actually reaches a minimum for an intermediate x value[50]. It was also found that the conductivity does not depend on the growth conditions like power and hydrogen dilution, but only depends on the Ge fraction. It is interesting to note that the ratio of photo to dark conductivity is close to

unity beyond x=0.75. The monotonous decrease of photoconductivity with incorporation of Ge indicated the degradation of minority carrier lifetime, which is very detrimental for the performance of solar cell devices.

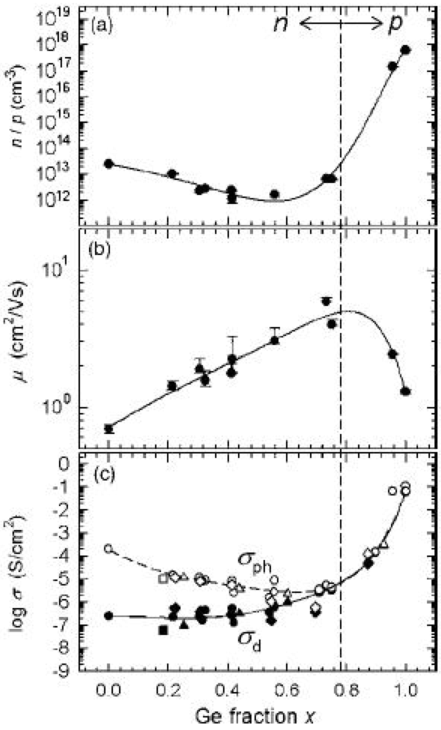

Figure 2.12 Transport properties of μc-(Si,Ge):H measured at various Ge compositions[49]

2. Matsui et al.[51], studied the Ge fraction as a function of GeH_4 concentration in the gas phase, defined as $[GeH_4]/[GeH_4]+[SiH_4]$. As GeH_4 concentration increases initially, the Ge fraction x rises drastically to 0.8 and then slowly increases to 1. By fitting a mathematical to this data it was proposed that the Ge incorporation efficiency from GeH_4 was five times greater than Si from from SiH_4. The preferential incorporation of Ge suggest that the Ge precursors have higher generation rate and surface reactivity compared to those of Si. This can be partially attributed to the lower dissociation energy and lesser thermal stability of the Ge-hydrides and Si-hydrides. Also it was reported that the growth rate of μc-$Si_{1-x}Ge_x$:H increases by a factor of 2 when power is increased from

10W to 30W and saturates beyond this point. But the Ge fraction does not depend on power. Also the growth rate of μc-(Si,Ge):H was found to be approximately equal to the sum of the growth rates of μc-Ge:H and μc-Si:H. This indicates that the film growth rate is determined by the individual growth rates of Si and Ge precursors. This might also indicate that the film composition might also be dominated by Si-Si and Ge-Ge crystallites rather than Si-Ge crystallites. But this particular paper does not provide any Raman data to support their argument.

3. Houben et al[55], studied the Raman Spectra of μc-(Si,Ge):H for various Ge contents fabricated by PECVD as well as SPC(solid phase crystallization). They concluded that the Raman peaks are broadest for Ge concentrations around 50% because ”the diversity of tetrahedral units” is maximum at 50% Ge concentration. This means that at high Ge contents good crystallinity of Ge-Ge crystals can be achieved and minimum FWHM of Si-Si peak can be observed at lower Ge contents. They also observed significantly sharper Raman peaks in SPC films compared to the PECVD films which indicated more random local variation in the films besides the variation of bond angle and bond lengths in the PECVD films.

   Cross-sectional TEM micrograph of a PECVD grown μc-(Si,Ge):H film is shown in Figure2.13. We see heterogenous phase growth i.e crystallite grains embedded in amorphous phase. The initial nucleation of μc-(Si,Ge):H and the columnar growth is believed to deteriorate because of the addition of *Ge*.

4. TEM and Raman studies were also performed by Miyazaki et al [54]. From Raman versus thickness of the films it was concluded that the amorphous-incubation layer thickness was 25nm as compared to 5nm in μc-Si:H. The same conclusion was also made from the TEM studies. From SIMS profiles it was shown that the composition of the films are uniform along at various thicknesses of films.

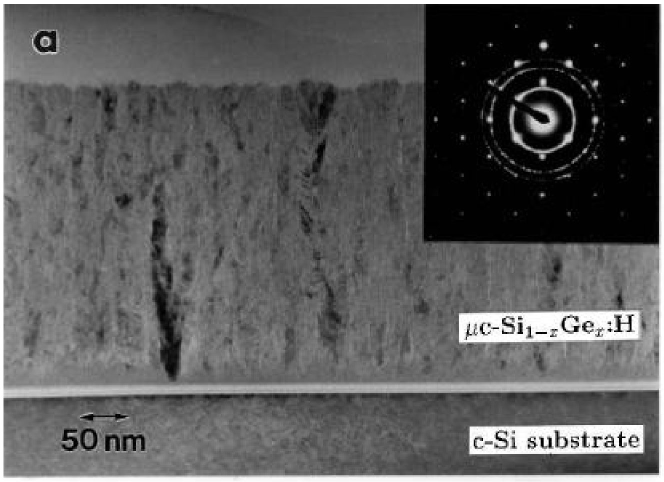

Figure 2.13 Cross-sectional bright-field transmission electron micrograph of the PECVD grown $\mu c - Si_{1-x}Ge_x$:H with x =0.52[55]

2.2.2.2 Growth mechanism

Ganguly et al.,[56] performed systematics study of effect of PECVD deposition parameters on μc-(Si,Ge):H like hydrogen dilution, power, pressure and temperature. From the studies of grain size versus hydrogen dilution done at different temperatures, it was found that at each temperature there is an optimum hydrogen dilution for maximum grain size, as shown in Figure2.14. It should be noted that at 250°C grains as large as 55nm were obtained using a silane to germane flow ratio of 0.9sccm to 0.1sccm at the optimum hydrogen dilution. The presence of optimum hydrogen dilution suggests that hydrogen atoms (or ions) participate both in reactions leading to the formation of crystallites and also in ion bombardment which disrupts the crystal growth. The balance between these two reactions leads to the largest crystallite formation, at a particular temperature.This can be better understood from the two reactions which represent the effect of hydrogen atoms/ions.

$$Si{-}H + H \Longrightarrow Si - + H_2 \tag{2.1}$$

$$Si - + H \Longrightarrow Si - H \tag{2.2}$$

Another interesting trend observed was that the optimum hydrogen dilution reduces with increasing temperature. This means hydrogen provides alternative source of energy at low

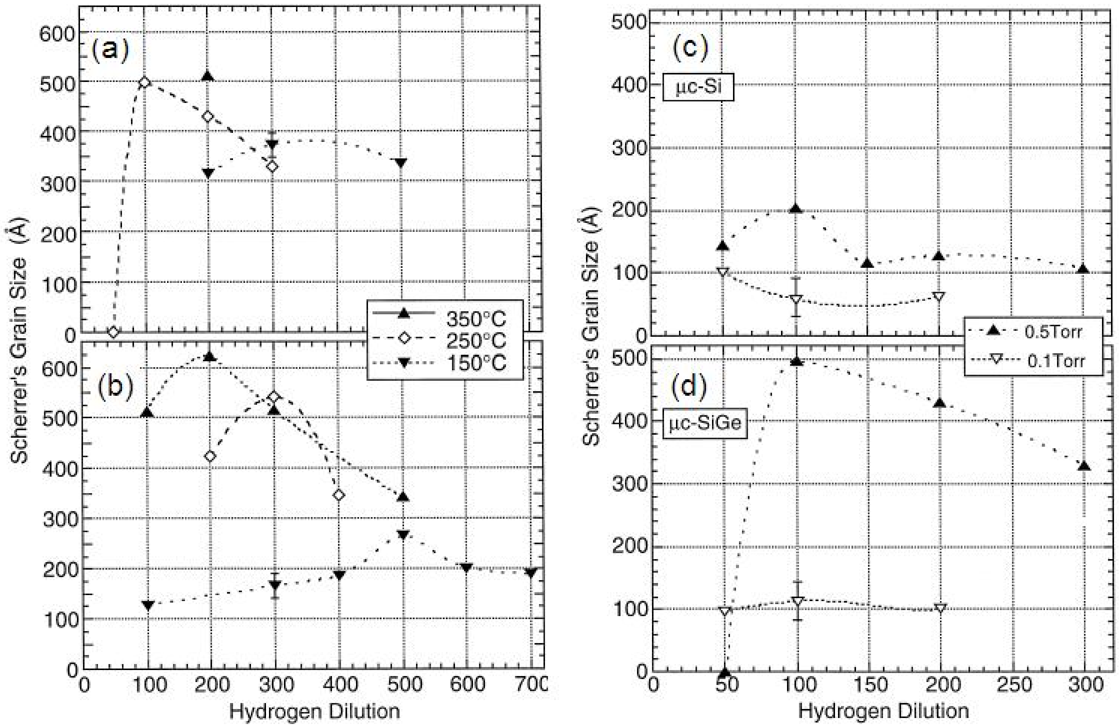

Figure 2.14 Grain sizes versus hydrogen dilution for different power (a)89mW/cm^2 and (b)637mW/cm^2. Figures (c) and (d) compare grain sizes of μc-Si:H and μc-(Si,Ge):H respectively as function of hydrogen dilution at 250°C using different pressures[56]

temperatures leading to the formation of bigger crystals. Beyond the optimum dilution, the detrimental effect of hydrogen is reversed at higher temperature which means that the rate of dissociation of $Si-Si$ bond by H_2^+ is dominated by thermal desorption of the hydrogen from $Si-H$ bond. If the ion flux is unchanged the former effect remains constant but with higher temperature, the latter becomes dominant resulting in the formation of bigger crystals. Also since the Ge-H bond is weaker compared to Si-H bond, surface desorption of H_2 from $Ge-H$ bond is easier which explains the higher grain size seen in nc-Ge:H[57].

Figure2.14 also shows the study of grain size versus hydrogen dilution at different pressures for μc-(Si,Ge):H and μc-Si:H. The formation os crystallites in μc-(Si,Ge):H is seen start at higher hydrogen dilutions compared to μc-Si:H which again confers with the explanation given in the previous paragraphs.

2.2.2.3 Device results

In this part we would review some of the important results reported from photovoltaic devices made with nc-SiGe:H as the base layer.

- Isomura et al.[58, 59], reported a solar cell with 5.6% efficiency with a nc-SiGe base layer as thin as $0.5\mu m$ with Ge concentration of 20%. Even though the Fill factors were in the range of 55-60, because of high short circuit currents(I_{sc}) like 20-25mA/cm^2 high efficiency could be achieved. The higher I_{sc} was attributed to the higher absorption in infrared region, for example a collection efficiency of 20% was observed even at 1200nm. Also the thinner devices reported here indicate the possibility of making thinner microcrystalline solar cells without sacrificing light absorption.

- Matsui et al.[49] reported photocurrents of > 27.4mA/cm^2 under reverse bas voltages. Even though improvement of infrared collection is observed by incorporation of Ge, that increment did not increase much with higher amounts of Ge in the material. Apart from this, a drastic loss of low wavelength Q.E was seen in devices with high Ge content. The efficiencies reported were 3.4% and 0.3% at 21% and 55% Ge composition respectively. Also devices with more than 60% of Ge exhibited electrical shunting. They observed electron collection problem in their substrate-type devices which was seen as improvement in low wavelength Q.E at reverse bias voltages. Reduced electron lifetime was suspected to be the possible reason.

- Rath et al [60] reported current densities of 9mA/cm^2 in μc-(Si,Ge):H devices with the base layer as thin as 150nm without any backreflector and a good V$_{oc}$ of 0.43V was also obtained with a high Ge concentration of 60%. Because of the moderately high deposition rate(0.75$\mathring{A}$/s) achieved this material was proposed as promising future alternative for μc-Si:H wherein high thicknesses are required to achieve the same current densities beause of the lower absorption coefficient. From XTEM studies they observed that the films deposited at higher power had higher void content and was concluded to be the reason for lower strain in the grains of the films made at high power. Even though moisture has been observed to accumulate in voids in microcrystalline films, these films were found to be intrinsic(from the Fermi level measurement)

Though several groups have reported solar cells with μc-(Si,Ge):H as the absorber layer, it is still not clear if the growth of μc-(Si,Ge):H follows a three step growth procedure as μc-Si:H (discussed in a previous section). It has been observed that though higher germane content increases the absorption coefficient it also degrades the transport properties like diffusion length and minority carrier lifetime. Also another important issue is to understand the effect of the presence of the three different kinds of crystallites ($Si - Si$, $Ge - Ge$ and $Si - Ge$) on transport properties.

2.3 Measurement techniques of Transport properties

In this section we will review the measurement methods developed for diffusion length and lifetime from literature. We will not be covering mobility in this discussion.

2.3.1 Diffusion length

Diffusion length is one of the basic material properties of a-Si and nc-Si. In nc-Si because of the columnar structure we have anisotropy in transport in different directions, for example the ambipolar diffusion length parallel L($\|$) and perpendicular L($\perp$) are different. L($\|$) can measured using a coplanar geometry, by steady-state photocarrier grating(SSPG) method [61, 62, 63]. L($\perp$) is reported in literature from surface-photovoltage measurements [64], which will be briefly reviewed here.

Surface photovoltage method(SPV)

The device structure used for SPV experiments is shown in Figure 2.15. The film under experiment is sandwiched between two electrodes. For example in the figure shown here a $/mu$Si:H film of 10$/mu$m is grown on a c-Si substrate. The top contact is a combination of SiN film and a TCO. Light of sufficient energy(more than the bandgap of the material) is illuminated through the TCO. A voltages drop (U_{oc}) is developed across the electrodes. L(or L($\perp$)) is evaluated as the x-intercept of the plot of I_0 versus α^{-1} while maintaining a constant photovoltage. One such plot is shown in Figure 2.15. Similar method of diffusion length calculation is also discussed in [66].

In this thesis we are using the reverse bias quantum efficiency method which will be discussed ind detail in the next chapter.

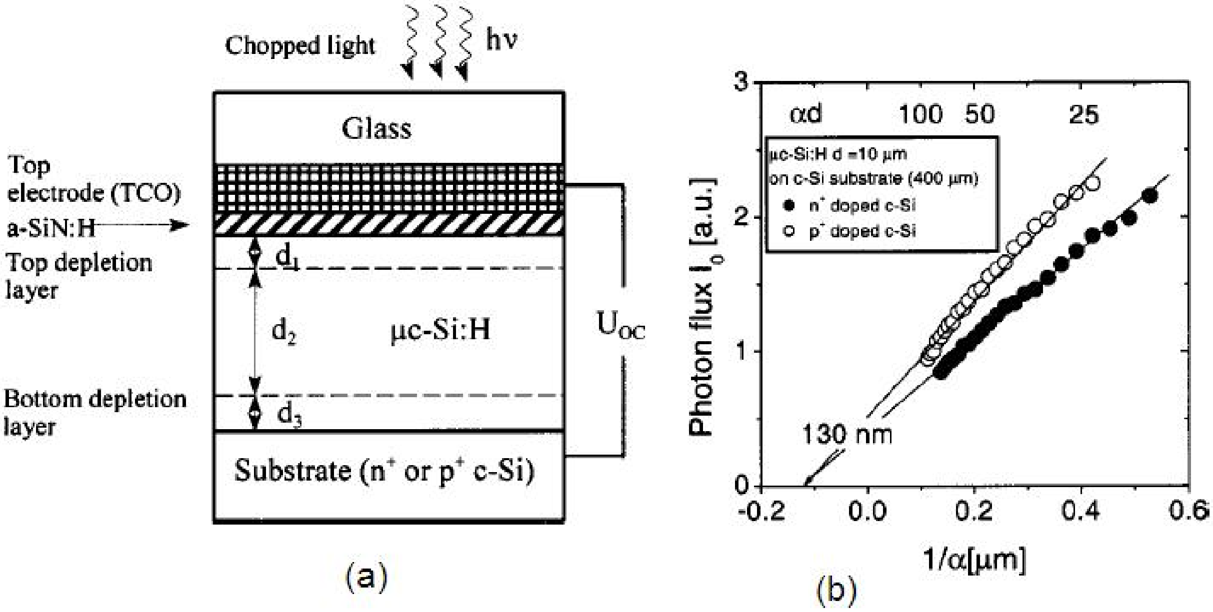

Figure 2.15 (a)Schematic of the device structure used for SPV experiment (b) Plot of I_0 Vs α^{-1} for a μSi:H film deposited on n-type and p-type Si substrates [65]

2.3.2 Minority carrier lifetime

Understanding the carrier transport and quantizing the associated properties like mobility,diffusion length, lifetime and conductivity are equally important to make better use of the non-crystalline materials [67, 68]. Conventional methods may not be applicable to a-Si:H or μc-Si:H because of their anisotropic growth, mixed phase(amorphous + microcrystalline) and partly porous nature[69, 70]. Also most of the characterization techniques measure properties like mobility and conductivity in directions perpendicular to growth direction, which is clearly inappropriate for our research since relating mobility in different direction in these anisotropic materials is not easy. Also some of these properties are strongly dependent on substrate material. Since we are interested in device structures it is necessary we develop techniques that are applicable to device structures.

The main objective of this work is to develop the RR technique to measure minority carrier lifetime in nc-Si:H and nc-(Si,Ge):H materials. We did not find any reports prior to this work, to the best of our knowledge, measuring this parameters in nanocrystalline or microcrystalline materials. Below I summarize some of the previous papers on lifetime measurement in crystalline or multicrystalline silicon.

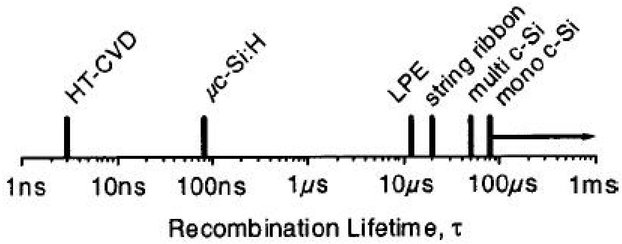

Figure 2.16 Comparison of recombination lifetimes in various forms of Silicon

- Mulati et.al reported lifetime measurements in multicrystalline silicon(Mx-Si) to be in the range of 20 -100μs using RRM. An interesting feature in this work was that they included the effect of surface recombination by carrying the experiments on mesa structures of various sizes and fitted the data to equation 2.3.

  $$\frac{1}{\tau_n} = \frac{1}{\tau_{bulk}} - s_P \frac{P}{A} \tag{2.3}$$

  The value in Mx-Si:H is much higher than what we can expect in nc-Si:H, which can be deduced from the graph in Figure2.16[49], a plot of simulated and experimental values of lifetimes in various materials.

Lifetime is one of the few parameters which directly depend on the purity of a crystalline semiconductor. Its measurement can detect defect densities as low as 10^{10} -10^{11} cm-3 [71] and is considered as a ”process cleanliness monitor” in the IC industry. The main challenge comes from the fact that we often have surface as well as bulk recombination giving rise to two lifetimes and our a measurement technique is likely to gives us the effective value. The result of an experiment can be affected by various surfaces, interfaces (as in a p-n junction or p-i-n structure in solar cell), doping and defect densities and density of carriers besides the properties of the semiconductor itself. It is important to notice the lifetime is the property of the carrier in a semiconductor rather than the semiconductor itself. This is the reason why different experiments can result in different values of lifetimes in the same material. This parameter has equal importance in the materials used in PV devices also. In a solar cell device lifetime of hole can be simply understood as the average time between a hole is generated from an EHP (electron-hole pair) generation and its recombination when it encounters a grain boundary or any other kind of defect.

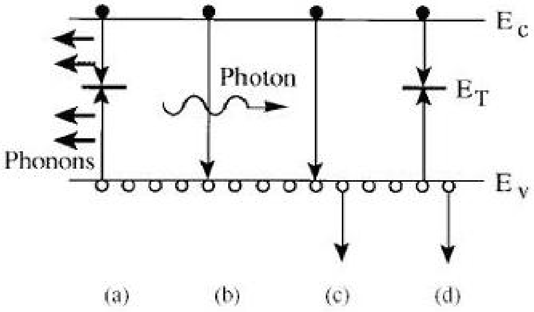

Figure 2.17 Recombination mechanisms (a) SHR (b) radiative (c) direct auger (d) trap- assisted auger

The different types of recombination possible are explained in Figure 2.17 [71] for a p-type semiconductor. It can be seen that SRH recombination takes place when we have trap levels in the band gap. In radiative recombination the electron directly recombines with a hole in the valence and then energy difference is released as radiation. This process has more probability in direct band gap semiconductors since phonons are not involved. In Auger recombination, for example, in a n-type semiconductor one electron gives up its extra energy to a second electron in the conduction band and recombines with a hole. The excited second electron releases its energy in the form of phonons (in one or several steps) and returns to E_c level.

Auger recombination dominates only when the injected carrier density or doping is high and the lifetime is proportional to $1/n^2$. From this discussion it is clear that under normal doping conditions, in nanocrystalline silicon the dominant recombination mechanism would be SRH-trap-assisted recombination.

The SRH lifetime is given by

$$\tau_{SRH} = \frac{\tau_p(n_0 + n_1 + \Delta n) + \tau_n(p_0 + p_1 + \Delta p)}{n_0 + p_0 + \Delta n}, \tag{2.4}$$

where p_0 and n_0 are the equilibrium hole and electron densities, Δn and Δp are the excess carrier densities and n_1, p_1, τ_n and τ_p are defined as

$$n_1 = n_i e^{(E_T - E_i)/KT} \qquad p_1 = n_i e^{-(E_T - E_i)/KT} \tag{2.5}$$

$$\tau_p = \frac{1}{\sigma_p \upsilon_{th} N_T} \qquad \tau_n = \frac{1}{\sigma_n \upsilon_{th} N_T} \tag{2.6}$$

Under low level injection, in a p-type material the electron lifetime can be simplified as

$$\tau_n = \frac{1 + \frac{2n_i}{N_A} cosh\left(\frac{E_t - E_i}{kT}\right)}{\sigma_n \upsilon_{th} p_o} \tag{2.7}$$

It can concluded from this equation that when the trap levels are located near the midgap level,as is the case with the defects in nanocrystalline silicon, the lifetime is independent of the doping of the material. But the contribution of shallow defects to recombination increases with doping and their effect becomes comparable to deep defects for high dopings(>1E16cm^{-3}) as is the case with the solar cells.

2.3.3 Lifetime measurement techniques

In this section I will briefly discuss the various experimental techniques available to measure lifetime in device structures. Note that there are numerous other methods used on films, which are not covered here.

Diode current voltage

The total forward bias pn junction current can equated to the sum of recombination currents in space-charge region, quasi-neutral region and surface recombination.

$$J = J_{0,scr}\left(e^{\frac{qV}{nKT}} - 1\right) + J_{0,scr}\left(e^{\frac{qV}{nKT}} - 1\right) \tag{2.8}$$

where $J_{0,scr}$ and $J_{0,scr}$ are given by the equations

$$J_{0,scr} = \frac{qn_iW}{\tau_{scr}} \qquad\qquad J_{0,qnr} = qn_i^2F\left[\frac{D_n}{N_AL_n} + \frac{D_p}{N_DL_p}\right] \tag{2.9}$$

For a p^+n junction $J_{0,qnr}$ can be simplified to

$$J_{0,qnr} = qn_i^2F\frac{D_p}{N_DL_p} \tag{2.10}$$

But evaluation of F is complicated because it in turn needs diffusion length value and surface recombination velocity and reported several other pitfalls in its interpretation are reported in literature. Also we might need another experiment to evaluate F itself.

Open Circuit Voltage Decay(OCVD)

In this method a forward biased diode is abruptly subjected to open circuit condition and the decay of open circuit voltage is observed. After simplifying the original equations we can get

$$\tau_{rr} = -\frac{KT/q}{\frac{\partial V(t)}{\partial t}} \tag{2.11}$$

Reference[71] claims that this method may not be applicable for values of lifetime close to 100ns, beyond which it is difficult to achieve an ideal open circuit condition with low lifetime diodes. OCVD method is significantly affected by the junction capacitance and shunt resistance which imposes a restriction when intended to use this method in a solar cell structure.

Reverse recovery method

It was one for the first experimental techniques implemented to measure carrier lifetime. The experimental setup and the voltage, current waveforms are shown in a different chapter. In this method a diode in forward bias is switched abruptly to reverse bias, as shown in the schematic. But the stored minority carriers in the n layer (assuming we have a p^+n diode) cannot abruptly fall to zero concentration and hence diode voltage remains at $+V_f$ for some time (reverse recovery time, T_{rr}) and then it quickly falls to a negative value. Lifetime (τ) of the minority carriers (holes) is calculated as

$$erf\left(\sqrt{\frac{T_{rr}}{\tau}}\right) = \frac{I_f}{I_f + I_r} \tag{2.12}$$

where I_f and I_r are the forward and reverse currents. Reverse recovery method (RRM) has the following advantages compared to OCVD method

- Ensuring ideal open circuit condition(OCVD) is difficult compared to obtaining a voltages reversal (RRM)

2.3.3.1 Temperature dependence of Lifetime

Several researchers have reported results from TDLS (Temperature dependent Lifetime Spectroscopy) used in defect characterization, for example in studying the location of the defect levels. Rein et al, discussed in detail the methodologies for TDLS and IDLS (Injection dependent Lifetime Spectroscopy) in [] based on systematic analysis of SRH theory and equations for recombination lifetime. They also pointed out the limitations of these two methods. We briefly discuss the results from TDLS here.

The actual equation for SRH lifetime can be simplified under low level injection(LLI) level for a p-type semiconductor to

$$\tau_{SRH}^{LLI,p} = \tau_{n0}\left[\left(1 + \frac{p_1}{p_0}\right) + k\left(\frac{n_1}{p_0}\right)\right] \tag{2.13}$$

where k is the capture assymetry factor given by,

$$k \equiv \frac{\sigma_n}{\sigma_p} \tag{2.14}$$

As postulated in [69], "Deep defects with energy levels close to midgap are most effective for recombination. The resulting LLISRH lifetime is independent of the doping concentration and equals the minority capture time constant. The SRH recombination rate is limited by the capture of minority carriers.Shallow defects with energy levels several kT away from midgap only contribute to recombination for high doping concentrations."

From a temperature perspective the lifetime equation can be re-written as

$$\tau_{SRH}^{LLI,p}(T) = \tau_{n0}(T)\left[1 + k\frac{n_1(T)}{p_0}\right] \tag{2.15}$$

Substituting for $n_1(T)$ and further simplification leads to an equation like 2.16

$$ln\frac{\tau_{SRH}^{LLI,p}(T)}{T} = const - \frac{E_c - E_t}{kT} \tag{2.16}$$

As shown in Figure2.18, beyond the onset temperature we see an linear Arrhenius increase of lifetime. The onset temperature shifts to higher values for deeper trap levels. In the extreme case of midgap defects we see the absence of onset temperature and the decrease we see is solely because of the τ_{n0}. It was also concluded that the onset temperature decreases to lower values with decreasing doping or increasing k, because either of these defects lead to reduced recombination activity.

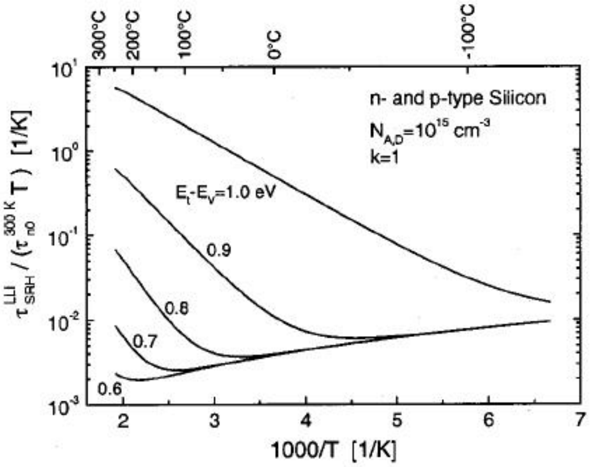

Figure 2.18 Effect of energy level E_t on linear Arrhenius increase of temperature dependent normalized LLI-SRH lifetime, for k(asymmetry factor)=l

CHAPTER 3. GROWTH AND CHARACTERIZATION

In this chapter we discuss fabrication of films and devices is done and also the various techniques used in the corresponding analysis. Even though the final aim is to the measurement of transport properties in solar cell structures, to make successful PV devices we first need to do a film analysis in which we deposit a single film of nc-Si or nc-SiGe on a glass or SS(stainless steel) substrate and check for the crystallinity, grain size or conductivity. Once optimized, this film will become the base layer for the actual PV device. Here we first discuss the film analysis experiments: Raman spectroscopy, X-Ray diffraction spectroscopy and conductivity measurement. We then discuss the various device experiments. To start with, a brief discussion of the VHF PECVD reactor is also included.

3.1 VHF PECVD Reactor

The cross sections of the PECVD reactors used for the experiments of this thesis are shown in Figures 3.1 and 3.2. Even though two reactors are used, a detailed description is only given for R1 since both the working principle is same behind both the equipments. R1 is used for non-doped layer depositions like the base layers of the solar cell. R2 is used for heavy doped layers like the n+ and p+ layers. As can be seen, it would be difficult to deposit all the layers in a single reactor, since the dopant accumulation on the reactor walls from the dopant layers will make it difficult to attain good crystallinity, essential for the base layer. These reactors are capacitively coupled with RF voltage applied across the two electrodes, as can be seen in Figure 3.1. The top-grounded electrode is nothing but the sample holder itself, with the RF power being received by the bottom electrode. The power starts from a function generator(8116A HP, 50MHZ) as a square wave of 46MHz, with peak voltage of

540mV for a nanocrystalline layer or 200-300mV for an amorphous layer deposition. It is then amplified by a power amplifier(operable in Frequency range: 250KHz-150MHz) and is given as the input to a matching circuit, which when properly tuned will ensure maximum power transfer to the reactor, which can be thought of as a waveguide. The tuning is performed using a Ameritron ATR-20 antenna tuner, through which we control both the capacitances as well as the inductance.

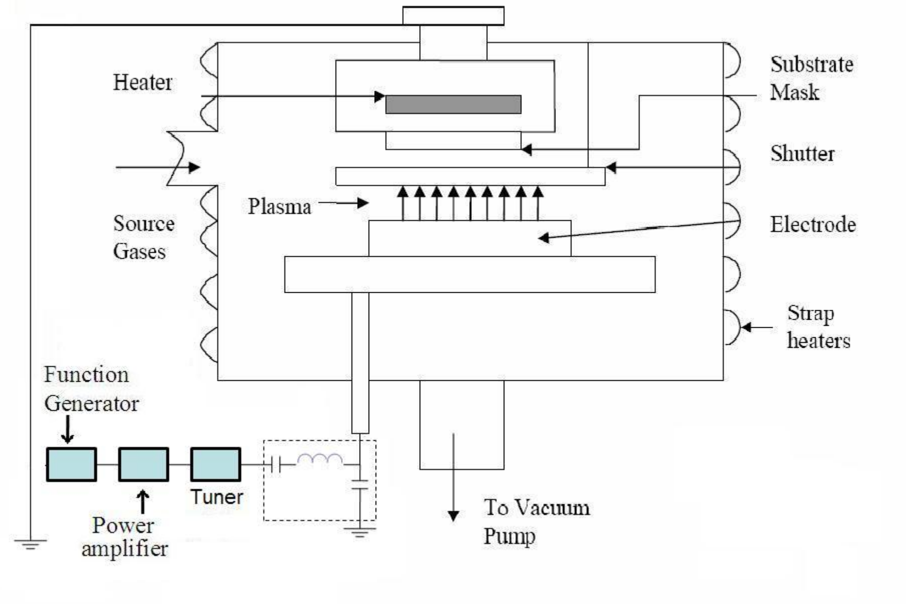

Figure 3.1 Schematic of the VHF PECVD reactor(R1)

The source gases enter the reactor through the sidewalls, and the vacuum pumps are attached at the bottom, right below the RF electrode. As any other high vacuum system, this setup has a two sets of pumps: mechanical and turbo vacuum pump. Mechanical (Roughing) pump is an oil diffusion pump meant for reducing the pressure from 1atm to 1Torr range. The turbomolecular pump has the capability of reducing the pressure from 1Torr to 10^{-6}Torr range, the normal base pressure we aim for before starting any deposition.This pump work on the principle that gas molecules can be given momentum in a desired direction by repeated collision with a moving solid surface (combination of rotors and stators in this case). A turbo pump in turn needs a mechanical pump near the exhaust since it cannot be exposed to the atmospheric pressure directly. Note that both the mechanical pumps used in this setup are similar to each other. Whenever the substrate holder is first loaded, we give several N_2 purges so as to attain the μTorr pressure quickly. Once we attain the required base pressure we start the required gases and ignite the plasma. Further explanations of how the vacuum systems work can be found in References [72, 73, 74] For convenience we always start the plasma at high pressure like 300mT and then reduce the pressure allowing the plasma to stabilize at the required pressure, power and gas flow levels. During this initial time, we cannot have the sample exposed to the plasma, hence we have a shutter below the top electrode. Note that the diameter of the electrodes and their separation are the most important parameters which decide the plasma characteristics besides the parameters like pressure and power levels, which we can vary from run to run. It was observed that loading the n^+ and heating the reactor walls overnight resulted in reduced defect density.

The plasma characteristics depend on the power delivered to it and the gas/pressure ambient maintained inside the reactor. To record the power going in we have a power meter which shows the input and reflected power. For a particular gas flow and pressure, if the tuning is performed correctly, every input rf voltage will correspond to a maximum deliverable power to the reactor, which can understood as a waveguide. The net power going in is proportional

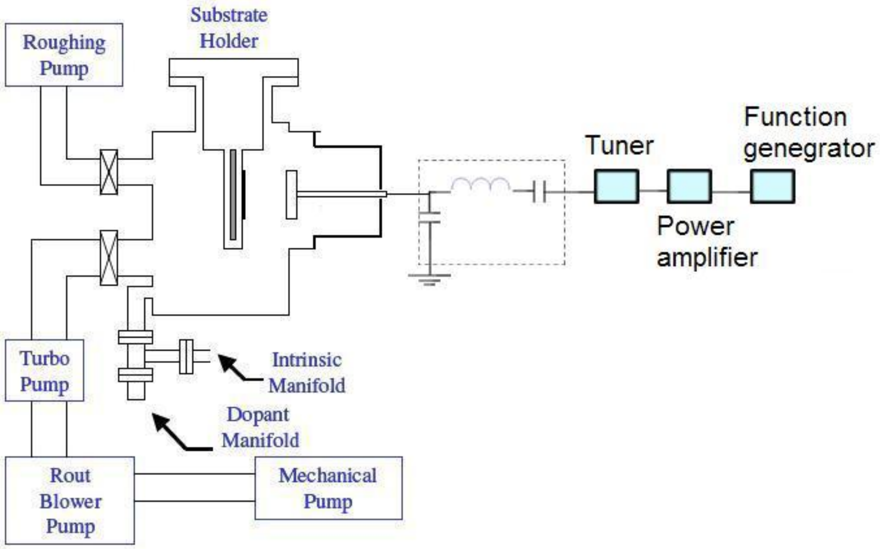

Figure 3.2 Schematic of the VHF PECVD reactor (R2)

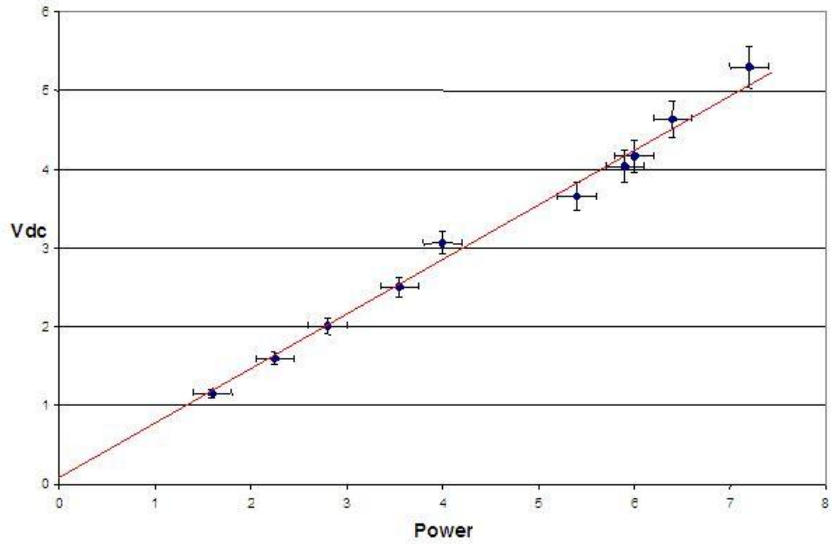

Figure 3.3 Plot of Vdc versus RF power showing proportionality

to the square of the rf voltage(measured by the rf probe) and is also directly proportional to the dc voltage developed on the bottom electrode.

Figures 3.3 and 3.4 demonstrate this behavior, for this particular example the measurements were made at the following conditions: pressure = 60mT, frequency = 45.7MHz, gas flows, $[H_2]$=$[SiH_4]$=30mT. Note that frequency is one of the tunable parameters and can be considered to be the part of tuning circuit(other than C1,C2 and L), but it is only varied within a range of 1MHz around 46MHz. This range of frequencies are selected depending on the reactor design and hence we should not vary the frequency by a huge value. In Figure 3.4 note the straight line fit of log(power) versus log(Vrf) has a slope of 2 as expected. At the end of tuning we always aim for 1)Minimum reflected power, 2)Maximum DC voltage and 3)Maximum peak-to-peak voltages read from the RF probe and resistors. Thus we have several parameters to make sure that we have repeatability in our runs. A more detailed discussion of the plasma theory can be found in References [75, 76, 77].

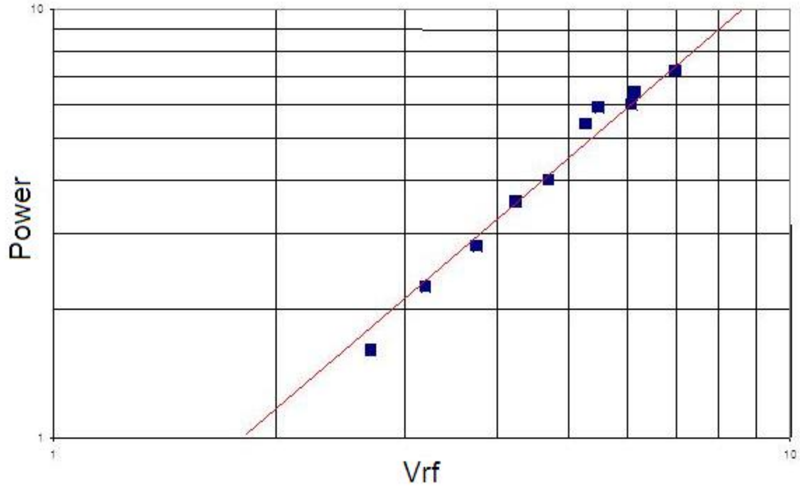

Figure 3.4 Plot of RF-power versus RF voltage on a log scale. The straight line fit has a slope of 2

3.2 Film Characterization

The films for both Raman and XRD spectroscopy are deposited on SS substrates. Since the properties of nc-Si or nc-SiGe are proven to depend on the substrate, we deposit a thin layer or a-Si and then do the nanocrystalline film deposition. The total film needs to be 0.5-1um thick for these measurements. On the other hand for conductivity measurement the films are deposited on glass substrate.

3.2.1 Raman Spectroscopy

Raman scattering is an interesting light scattering technique in which light of a known frequency and polarization is incident upon a sample [78]. The scattered light is shifted in frequency with respect to excitation frequency, whose value is uniquely dependent on polarizability molecule. As quoted in [78], ”in order to be Raman active, a molecular rotation of vibration must cause change in a component of the molecular polarizability(either magnitude or direction of polarizability ellipsoid)”. We used a 488nm laser in an inVia Reflex Raman microscope manufactured by Renishaw. The acutal results from these experiments will be discussed in the next chapter.

3.2.2 XRD(X-ray Diffraction Spectroscopy)

We used a Siemens X-ray diffractometer to determine the crystallite sizes in various orientations in the nanocrystalline materials [79]. In an XRD experiment when the incident x-ray's wavelength is equal to the distance between the crystal planes, we satisfy Bragg's law and a peak in diffraction spectrum is observed. The raw data is then de-convoluted in the software: JADE 7.5. We can obtain FWHM and center of each peak and then use Scherrer's formula to calculate the grain size, as given in equation, where d is the grain size, β is the FWHM, $\lambda$is the wavelength and θ is the incidence angle of the x-rays.

$$d = \frac{0.9\lambda}{\beta cos\theta} \tag{3.1}$$

The XRD profiles of the nc-SiGe film, shown in Figure 3.5 indicate the dominant peak to be $< 111 >$. The deposition conditions were p = 50mT, T = 250^{o}C, H2 flow rate = 87sccm, [SiH4]:[10%GeH4] = 1:6. Grain sizes calculated form Scherrer's formula from the $< 111 >$ and $< 220 >$ peaks are 13nm and 8nm respectively. It was found that when the film was grown at 300^{o}C $< 111 >$ grain size remained same while that of $< 220 >$ increased to 12nm.

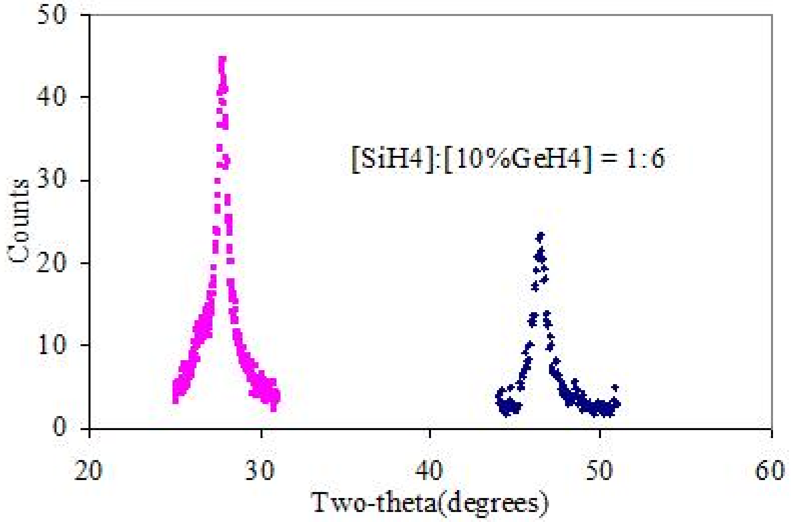

Figure 3.5 XRD Spectrum showing $< 111 >$ and $< 220 >$ peaks on nc-(Si,Ge) film

3.2.3 Conductivity Measurement

For this measurement we deposit films of thickness 0.5μm or more and then evaporate chromium contacts followed by smearing of Silver paint on top of chromium contacts. Since the work functions of chromium and silver are 4.52eV and 4.7eV respectively and the electron work function of silicon is 4.5eV Silver helps in obtaining a more ohmic type of contact since the the work function is more close to the fermi level in the semiconductor (4.5+0.5=5.0eV). Examples of Schottky and Ohmic contacts are shown in Figure 3.6. Also the conductivities of Cr and Ag are 0.0774*$10^6 cm^{-1}\Omega^{-1}$ and 0.63*$10^6 cm^{-1}\Omega^{-1}$. The conductivity is calculated using the equation 3.2

$$\sigma = \frac{l}{st}\frac{I}{V} \tag{3.2}$$

where l,s,t are the length, width (of the conductive film between the contacts) and thickness of the film respectively. We normally use two closely placed metal bars for the contacts where s/l =20. Since the presence of room light effects the conductivity, we have a large aluminum ”light impervious” box. Thee probes are connected to a Keithly 617 electrometer and a Keithly 230 voltage source to supply a 100V bias scross contacts and measure the resulting current. The signal comes out of the box in a triax cable, the design of which is extremely critical since we are measuring sub-nano amp current and 10% of error in I value will result in 10% error in conductivity.

The electrical properties measured in a nc-SiGe film with the deposition conditions, [H2] = 77sccm, [SiH4]: [10%GeH4] = 1:6, T = 275^{o}C, P = 50mT, RF power = 35W are given in Table 3.1. The activation energy of 0.518eV shows that the film is slightly n-type. Since no ppm doping of TMB is used the resultant n-type dopant film because of the default O contamination of the reactor is not a surprise. The dark conductivity and the ratio of dark to photoconductivity values are in good agreement with some of the previously reported values in the same material[51].

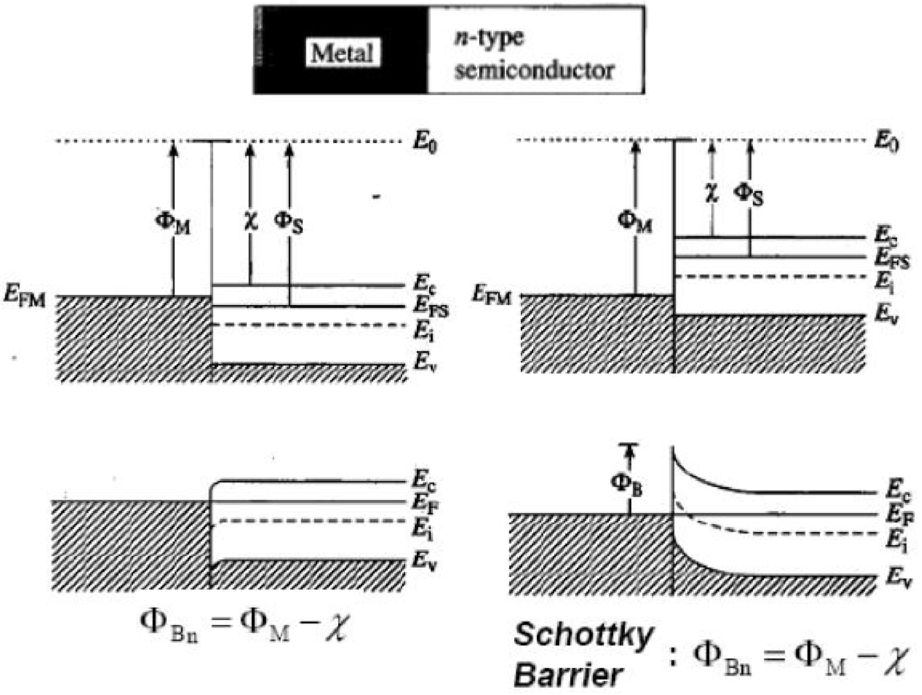

Figure 3.6 Band diagrams of Metal/Semiconductor before and after contact for Schottky and Ohmic cases.

Table 3.1 Conductivity and Activation energy measurement

Dark Conductivity	2.13 x 10^{-7} $(\Omega cm)^{-1}$
Photo Conductivity	3.06 x 10^{-6} $(\Omega cm)^{-1}$
Ratio(dark/photo conductivity)	14.4
E_a (activation energy)	0.518eV

3.3 Device structure

The cross section of the device structure is shown in Figure 3.7. The deposition starts on a SS substrate without any special back reflector. The first layer deposited is amorphous n^+ layer about 0.3μm thick. At the beginning of the base layer deposition, we start with a very thin a-Si film followed by a nc-Si film and then transit to the final required nc-(SiGe) film. The nc-Si layer helps in achieving a smooth transition of the band gap in the device. It was observed that extreme care has to be taken at the p-i interface in nc-SiGe devices, since we make a transition from nc-SiGe(i) to nc-Si(p+). Figure 3.8 shows the expected band diagram of a typical nc-SiGe device. The figure remains almost the same for a nc-Si device expect for the transition layers at the p-i and n-i interfaces. p^+nn^+ device structures were used

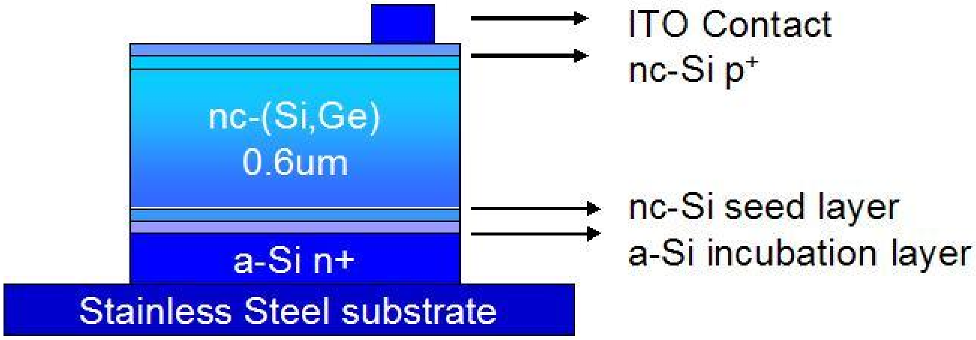

Figure 3.7 cross-section of the device structure

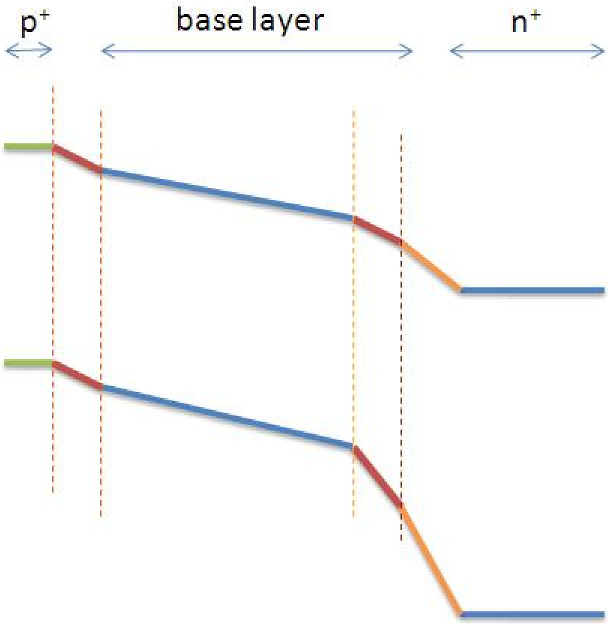

Figure 3.8 Approximate band diagram of the p^+nn^+ device

wherein the base n-layer is nc-(Si,Ge),n^+ and p^+ layers are a-Si and nc-Si respectively. All the depositions are done using VHF-PECVD systems at a frequency of 45MHz. While the intrinsic base layer was deposited in one reactor (R1), n^+ and p^+ layers were deposited in separate reactors to minimize the defect density and ensure better crystallinity.

The ITO contacts were deposited using a DC sputtering system [52]. DC sputtering can only be used to deposit conducting materials, where in ionized Ar ions are accelerated towards a target to remove the materials from its surface which then condenses on a substrate. The plasma is ignited using a mixture of Ar and 1%O_2/Ar. The thickness of the contact is 50nm. The calibration of the deposition parameters is performed by depositing the film on a 7059 glass substrate and measuring transmission and sheet resistance which define how well it can transmit the photons into the device (in the wavelengths of interest) and the quality of the Ohmic contact it can form. The choice of this material is itself justified because the work function of ITO is 4.8-5.1eV and the fermi in p+ layer is located 5.6eV below vacuum level. The minimum series resistance achievable with ITO top contact was found to be 50-60Ω. to further reduce, we used a Al bars on the ITO dot. Al provides 20% reduction in R_{series} but reduces the current.

3.4 Device characterization

3.4.1 I-V analysis

The I-V characteristic of a solar cell is the single important test that tells us almost the entire story of the device under test from the band gap of the base layer to interface problems. The important equations which define the performance of the device are listed below.

$$V_{oc} = V_T ln\left(\frac{I_L}{I_0} + 1\right) \tag{3.3}$$

$$F.F = \frac{V_m I_m}{V_{oc} I_{sc}} \tag{3.4}$$

$$\eta = \frac{I_m V_m}{P_{light}} = \frac{F.F V_{oc} I_{sc}}{P_{light}} \tag{3.5}$$

Open circuit voltage, V_{oc} depends on the photo current and the saturation currentI_0. Minimizing I_0 is one way to maximize V_{oc}, which can achieved by higher minority carrier diffusion lengths and higher doping concentrations in the base layer as inferred from the equation 3.6 [53].

$$I_0 = \frac{q n_i D_n}{N_A L_n} G_f \tag{3.6}$$

Here G_f is the geometry factor, a function of (t/L_n) and (S_∞/S_n). S_∞ and S_n are the recombination velocities in the bulk and edge of the p-layer (for an $n^+ - p$ device). For $S_\infty > S_n$, $G_f < 1$ which is helpful in reducing I_0. V_{oc} also depends on I_L (or J_{sc}). I_L can be calculated as the sum of the photocurrents from the individual layer of the device like emitter and base layers.

From a typical I-V curve of solar cell device, it can be seen that the power output of a solar cell depends on the bias point and Fill Factor indicated how this power compares to the actual *maximum* power output possible from the device. Fill factor can be maximized by the making the i-v curve more square like. The slopes of the I-V curve near Voc and Isc regions indicate R_{series} and R_{shunt} respectively. R_{series} depends primarily on the how good the ohmic contacts are and on the resistance of individual layers in the device. R_{shunt} depends on the leakage current through the surface or edges of the device and also on any direct leakage paths through the actual device itself(shorts).

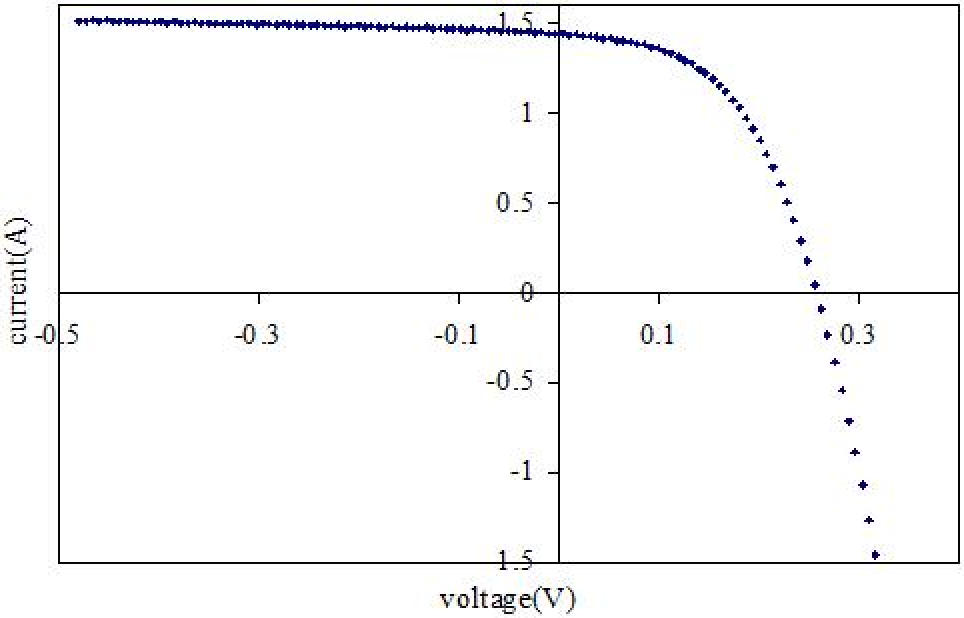

Figure 3.9 I-V characteristics of nc-(Si,Ge) device with Isc=1.43mA, Voc=0.258, FF=51

3.4.2 Quantum efficiency measurement

Quantum efficiency is defined as the ratio of number of carriers collected to the number of incident photons, per unit area per unit time. We measure it by shining the sample with a monochromatic beam and measure the current generated. The actual method used is a dual beam photocurrent method, for which the setup is shown in Figure 3.11. The monochromatic light beam passes through a 13Hz chopper and then is incident on the sample. The current generated from the sample is converted to voltage signal and is then detected using as phase lock amplifier. The sample is constantly soaked in a dc beam, which fixes the quasi fermi levels at a certain level so that the photo current generated is only from the monochromatic light. The frequency of the chopper is selected so that it is lesser than the frequency of the various signals in the electronic equipment in this setup and also the frequency of room light so that there is minimal noise by the harmonics. The normal scan of wavelength is done from 400nm to 900nm. Around 750nm we keep an extra filter in the path of the monochromatic light which can filter the lower wavelengths. We do this in order to avoid the effect of harmonics of some of the lower wavelengths. An example plot of Q.E is shown in Figure **??**, collected on a nc-SiGe sample. The collection efficiency reaches a maximum around 550nm and then

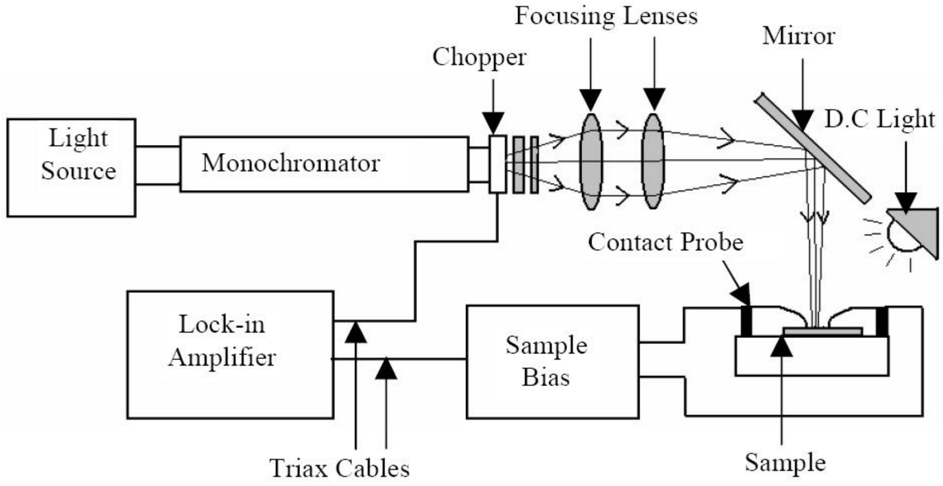

Figure 3.10 Experimental setup used for Q.E measurement using dual-beam photocurrent technique

quickly falls to 0.1 around 900nm. nc-Si being has slightly larger bandgap(1.2eV compared to 0.9-1.0eV), its Q.E plot will drop to 0.1 by 800-850nm. In these plots we normally plot *normalized* Q.E i.e, the values in the plot are normalized w.r.t the peak value, the maximum being 90% (remaining 10% is the reflection and absorption in the ITO contact). We use a reference solar cell to calculate the actual Q.E, using the equations

$$\frac{V}{A} \propto Q.E \tag{3.7}$$

$$Q.E_{device} = Q.E_{ref}\left(\frac{A_{ref}}{V_{ref}}\right)\left(\frac{V_{device}}{A_{device}}\right) \tag{3.8}$$

where V and A indicate the voltage signal and the active areas of the device or reference solar cell. Several important conclusions can be made from the Q.E curve. The collection at

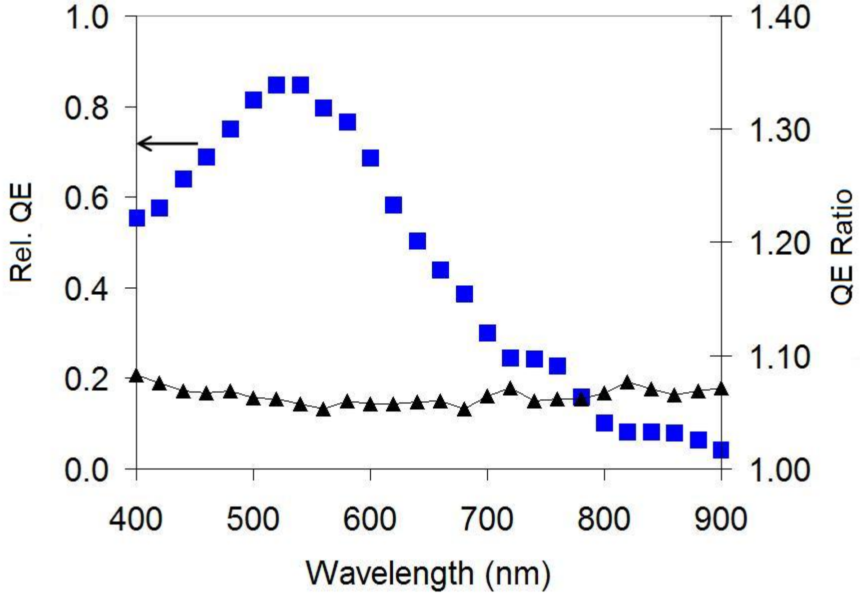

Figure 3.11 Experimental setup used for Q.E measurement using dual-beam photocurrent technique

lower wavelength corresponds to the absorption in the base layer closer to the p^+ interface. Similarly the Q.E signal in the infrared regime corresponds to the photons absorbed at $n^+ - n$ interface. We also measure the Q.E signal at 0V and -0.5V external bias. By applying reverse bias we are enhancing the electric field in the base layer, which if results in much higher carrier collection($> 5\%$) indicates that we have a potential barrier present in the device. Also from

Q.E data we can get an *estimate* of the J_{sc} of the device using the equation

$$J_{sc} = \sum_{\lambda} qF(\lambda)Q.E(\lambda) \tag{3.9}$$

3.4.3 Diffusion length measurement

We measure diffusion from simplified expression of quantum efficiency. QE consists of current components from space charge region and the base layer. The current from p^+ and n^+ regions is negligible because the minority carrier lifetime is very less in those regions and hence they cannot contribute to the total carrier collection. The first term in the following equation corresponds to the carriers collected from space charge region, wherein we assume all the carriers generated are collected. The second term corresponds to the collection from base layer outside the depletion region whose thicknesst_p is given by $t_b - W_d$, where t_b is the total base layer thickness W_d is the depletion width. Note that the depletion region in the p^+ region is neglected.

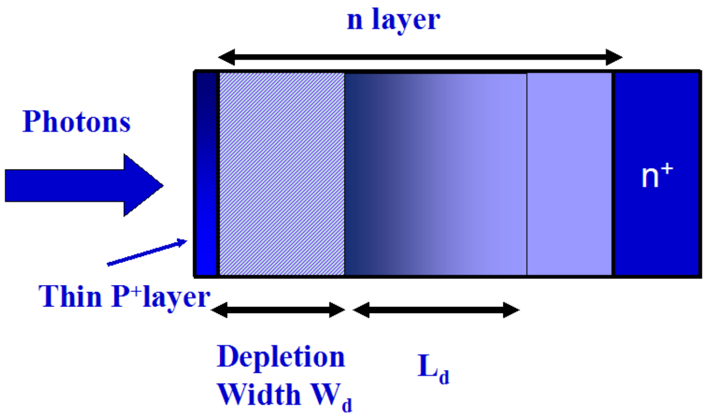

Figure 3.12 Depletion width in a solar cell device

$$\begin{aligned}
Q.E &\propto I_{SCR} + I_{baselayer} \\
&\propto 1 - e^{-\alpha W_d} + \int_0^{t_p} e^{-\alpha(W_d + x)} \alpha e^{-\frac{x}{L_p}} dx \\
&\propto 1 - e^{-\alpha W_d} + e^{-\alpha W_d} \left(\frac{\alpha L_p}{1 + \alpha L_p} \right) \left[1 - e^{-\frac{t_p}{L_p}(1 + \alpha L_p)} \right] \\
&\propto \alpha W_d + \left(\frac{\alpha L_p}{1} \right) \left[1 - e^{-\frac{t_p}{L_p}} \right]
\end{aligned}$$

Here the assumptions made are $\alpha W_d << 1$ and $\alpha L_p << 1$, which reduces to W_d,$L_p << 1/\alpha$. At 1050nm, α for μSi:H $0.1\mu^{-1}$ or $1/\alpha = 10$um. The value of W_d is always much less than 10um. If L_p is <2um, we can still say $L_p << 1/\alpha$.

The procedure for such a case would be to compare relative Q.E (which is nothing but the Q.E signal value) versus the calculated R.H.S of equation 3.10 (say, F). Their ratio (F/Q.E) should remain almost the same at various reverse bias values, if F is calculated assuming a correct value of L_p. One such calculation is shown in 3.2. F' is calculated as average value of $F/Q.E$ (over various reverse bias voltages) times F. We then plot F' and Q.E and observe that we obtain a fairly good fit for our guess of L_p as shown in Figure 3.13. Also we can compare the normalized plots of F' and Q.E,as in Figure 3.14 which also fit in a good manner.

Table 3.2 Calculation procedure for estimating L_p.

Q.E	F	F' = F*5.62	Normalized F'	Normalized QE
3.739	0.667	3.748	0.981	0.975
3.784	0.671	3.772	0.987	0.987
3.787	0.674	3.787	0.991	0.988
3.792	0.676	3.798	0.994	0.989
3.797	0.677	3.805	0.996	0.990
3.805	0.678	3.810	0.997	0.992
3.811	0.678	3.813	0.998	0.994
3.824	0.679	3.818	0.999	0.997
3.83	0.680	3.820	1.000	0.999
3.834	0.680	3.821	1.000	1.000
	<average> F/QE = 5.62			

Limitations of the method

A closer examination of the above method reveals that the diffusion length calculated does not have a high accuracy. The first reason comes from the mathematics behind equation 3.10. We are trying to fit an expression to measure Q.E signal. But the measured Q.E itself is varying in such small amount < 5%, even a wrongly fitted expression might look like scaling well with Q.E. Only if the measured values take huge variations, can we exactly check whether out fit is correct. Also, we observed while doing the calculations that, the expression is not very sensitive

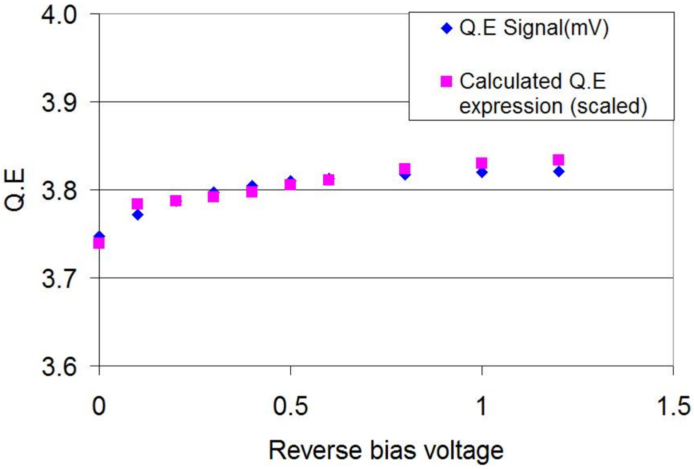

Figure 3.13 Comparison of Q.E and calculated F'

to L_p, which means the calculated L_p values do not have high accuracies. For instance in the calculation shown previously, the best fit L_p value was 3.65um. The ratio of F/QE for different reverse bias for this value was between 5.60 and 5.63. For L_p value of 6um the ratio still varies only between 5.59 and 5.63. This shows that even though we are aiming for the best fit, L_p values of ±20-30% still give similarly good fit. Also the multiplication factor between F and measured Q.E can be related to the other device parameters like back-recombination velocity which might be complicated to measure or calculate. That analysis was not included in this thesis, but if performed will give an accurate value of the diffusion length.

One more simplification possible to equation 3.10, is the case when $t_p >> L_p$. In that case the simplified expression would be equation 3.10. A plot of QE versus W_d would be a straight line with the x-intercept being L_p, as shown in figure 3.15. Upon the calculating L_p, we can perform a check whether the assumption $t_p >> L_p$ is correct.

$$RelQ.E = \alpha\left(W_d + L_p\right) \tag{3.10}$$

3.4.4 C-V analysis

Defect Density estimation

The capacitance versus voltage measurement (at low frequencies) was used to obtain the defect

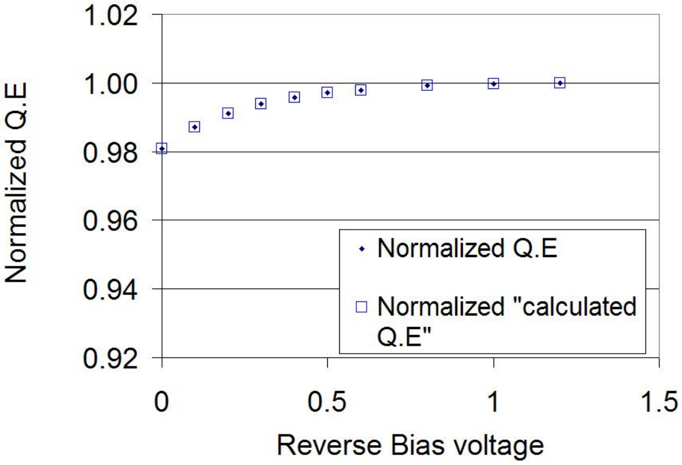

Figure 3.14 Comparison of normalized Q.E and calculated normalized F'

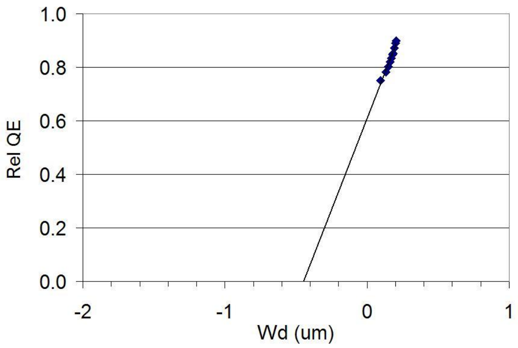

Figure 3.15 Calculation of Diffusion length from the x-intercept plot of relative QE versus W_d

densities. Applying the Kimerling's model and the procedure outlined in[82], shallow state (donor) and deep defect densities have been calculated. Two distinct straight lines are observed in the plot of $1/C^2$ versus V (reverse bias). At lower reverse bias we have the shallow defects responding to the capacitance measurements, while at higher reverse bias we have both shallow and defect densities contributing to capacitance. The shallow defects can be interpreted as donor density, which in our case is the O_2 dopant density from O_2 contamination. One such plot is shown in Figure 3.16. The low frequency is required since we need both the deep and shallow defects to respond to the measurement. One such plot is shown in Figure 3.16, where in the calculated values of N_d(doping density) and N_t(trap density) are 3.1E15cm-3 and

3.2E15cm-3 respectively.

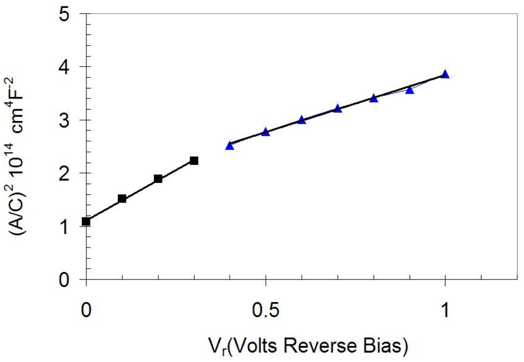

Figure 3.16 plot of $1/C^2$ versus V, showing two distinct linear regions

Multi-frequency C-V

From the above experiment, we estimate a value of trap density, but we do not get information about where the trap levels are exactly located. Such measurements can be made by performing C-V at various frequencies. This analysis has been detailed in Reference [80]. We plot the C-V curves at various frequencies. At low frequencies(1̃00Hz) we see two linear regions, but at high frequencies (1̃00KHz) we see the first linear region followed by a saturation of capacitance. At this high frequency we expect only the shallow defects(donor) to respond. Hence the situation is similar a crystalline silicon pn junction, as we increase reverse bias the depletion width increases and when the whole of base layer is depleted the capacitance saturates.

The frequency at which the change of the shape occurs in the capacitance curves can be interpreted as the frequency at which the escape frequency of electrons(υ) becomes much more than the capture frequency of holes.

$$\upsilon^{e^-}_{escape} >> \upsilon^{h^+}_{capture} \tag{3.11}$$

$$\upsilon^{e^-}_{escape} = \upsilon_0 exp^{\left(\frac{-(E_c-E_T)}{KT}\right)} \tag{3.12}$$

The transition frequency ($\upsilon^{e^-}_{escape}$) can be translated to the location of traps from equation 3.12.

CHAPTER 4. RESULTS ON FILMS AND DEVICES

In this chapter we discuss how the material analysis and device optimization has been performed. The discussion is limited to nc-SiGe devices.

4.1 Analysis of crystallinity

Figure 4.1 compares the Raman spectra of two films done at different ratios of flow rates of silane to 10% germane, other deposition conditions being p=50mT, T=300^{o}C, H2 flow rate = 77sccm. When the flow ratio is 1:6 ([SiH4]: [10%GeH4]), the ratio of crystalline to amorphous peak of Ge-Ge is 1:1. The same ratio becomes 2.2:1 when the flow ratio is 1:12. It was observed that the FWHM (full width at half maximum) of Si-Si peak does not change, but that of Si-Ge is lower in the case of more germanium indicating formation of more crystalline (Si,Ge). This indicates that we obtain more crystalline Si-Ge and Ge-Ge structures at higher germanium concentrations.

Some other observations made are listed below:

- Based on the variation in FWHM, it was observed that at higher temperatures 350^{o}C the crystallinity of Si-Ge and Ge-Ge reduced while that of Si-Si improved.
- At lower hydrogen dilutions the amorphous content in Ge-Ge peak increases and the SiGe and Si-Si peaks show higher FWHM, as expected.
- It should be noted that the hydrogen dilutions needed for nc-SiGe are much higher than that of nc-Si:H. To check the effect of hydrogen dilution, two films were made with different hydrogen flow rates 77scccm and 56sccm, but with same ratio of Silane to 10%germane (=1:12), other deposition conditions being P=50mT, T= 300^{o}C, RF power

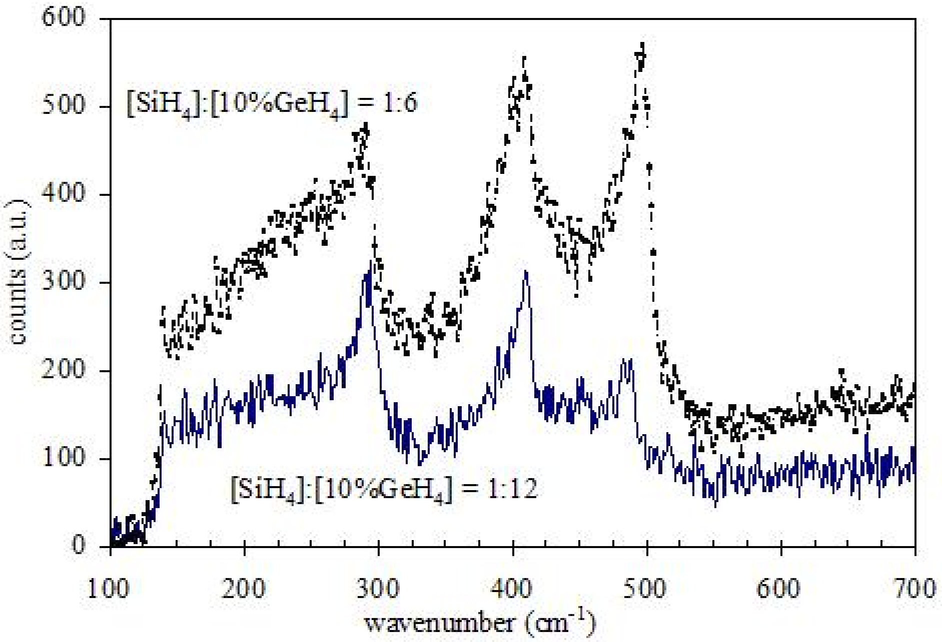

Figure 4.1 Raman Spectra for two nc-(Si,Ge) films with different Germanium contents

= 50W. The ratio of crystalline to amorphous peak of Ge-Ge reduces to 1.65:1 in case of lower hydrogen dilution from 2.3:1 in the other case.

- Also it was observed that the Raman spectrum showed little change when the RF power is increased from 30W to 50W.

4.2 Device structure

Several recipes were experimented to make successful solar cell devices using the above films as the base layers. Most of the devices were made using the deposition conditions: H_2 flow rate = 75sccm, T = 250^{o}C, p = 50mT, RF power = 30-35W. The typical i-layer thickness was 0.6-0.7m. While some of the devices were made with hydrogen grading technique where in the $i$layer is started with a high hydrogen dilution and then gradually reduced [6], some devices were made with graded B doping, by controlling the flow of ppm TMB. The former technique was demonstrated to increase amorphous phase as the thickness of i-layer increases[81], the latter was proven to provide better collection of the carriers because of the internal field it creates[10]. The I-V curve shown in Figure 3.9 has been obtained on a device made using the following ratio of the flow rates: $[SiH_4]$: $[10\% GeH_4]$ = 1:6.

Figure 4.2 compares the relative QE of a nc-SiGe device with that of a nc-Si device. Other than enhanced infrared absorption, we also see that the relative QE in nc-SiGe at lower wavelengths (400nm) is not degraded compared to nc-Si indicating that we do not have any electron collection problems, as was observed by other groups. It was also observed that the QE ratio between -0.5V bias and 0V bias was less than 1.05 which shows that the band gaps were well graded at both p-i and i-n interfaces and there are no potential barrier anywhere in the device. We should also note that even though relative QE looks to be higher in the entire wavelength range for nc-SiGe their current densities are still lesser than nc-Si devices, because of the overall crystallinity and degraded carrier transport properties.

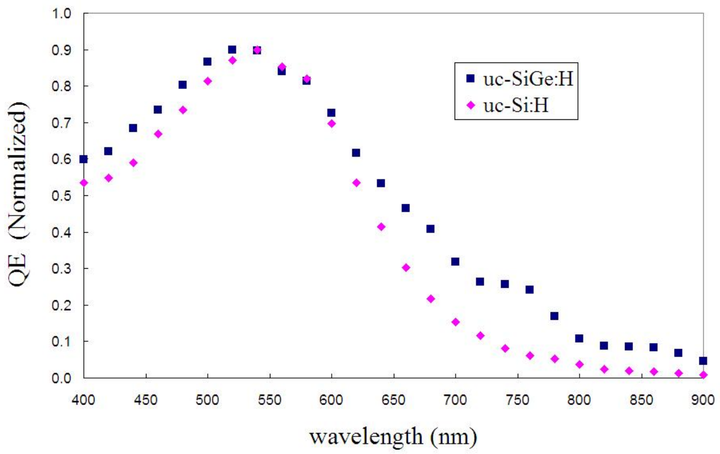

Figure 4.2 Comparison of relative QE between a nc-Si and nc-SiGe device showing enhanced absorption in infrared regime

4.3 Devices with varying germanium contents

In this section the device results obtained on nc-(Si,Ge) are presented. In the following we discuss how various device parameters like defect densities and V_{oc} have been observed to change as a function of germanium content.

4.3.1 V_{oc} and Q.E

A clear correlation was observed between the germanium content in the base layer and the open circuit voltage (V_{oc}) as well as the absorption of the device in the infrared region. Figure4.3 plots the V_{oc} and normalized Q.E at 900nm versus the parameter x, where x = [10%GeH4]:[SiH4]. This proves that for more germanium content we are obtaining a lower band gap material as was observed in literature also. The same effect is also reflected as higher absorption in the infrared region.

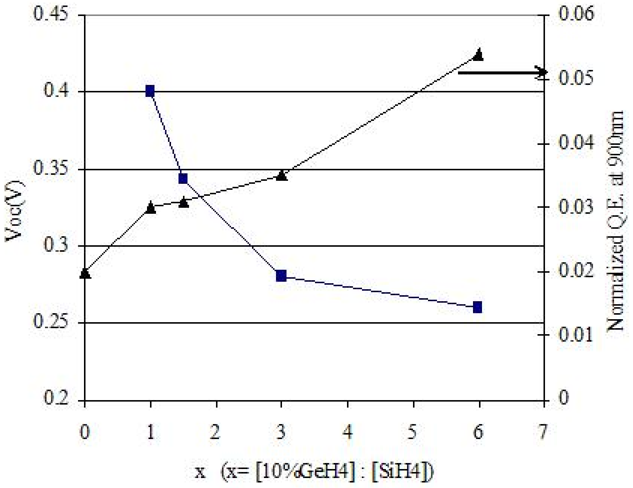

Figure 4.3 Variation of V_{oc} and normalized Q.E (at 900nm) versus parameter x, where x=[10%GeH4]:[SiH4]

4.3.2 Indicated Rshunt

It was also found that R_{shunt} increased at lower germanium contents indicating better crystalline structures.

4.3.3 Defect density

It was observed that devices with higher germanium concentration had relatively higher defect densities (7-9x$10^{16}cm^{-3}$), while lower germanium concentrations resulted in defect densities like 1-2x$10^{16}cm^{-3}$.

4.3.4 Dark I-V curves and crystallinity

The dark current was measured to estimate the reverse saturation current. Figure4.4 compares dark I-V plots from three samples whose details are given in Table4.1.

We can see that sample A shows a more crystalline structure than sample B because sample A shows two linear regions and follows the standard diode model with generation-recombination region and diffusion from the bulk. Sample A and Sample B were prepared under identical conditions except for different germane gas flows. So we can conclude that other conditions remaining same, as the germane gas flow increases the overall crystallinity decreases. Figure 4.4 also shows dark I-V plot of a nc-Si sample for comparison. The reverse saturation current in nc-(SiGe) (sample A) was found to be an order higher than nc-Si (sample C). This correlates well with the defect densities calculated from the C-V curves which were $4\text{x}10^{16}cm^{-3}$ and $3\text{x}10^{15}cm^{-3}$ respectively.

Table 4.1 Comparison of the device characteristics used for dark IV experiments

sample			Voc	Isc	FF
A	nc-(Si,Ge)	less germane content	0.393V	1.46mA	47.1
B	nc-(Si,Ge)	more germane content	0.277V	1.3mA	45.2
C	nc-Si				

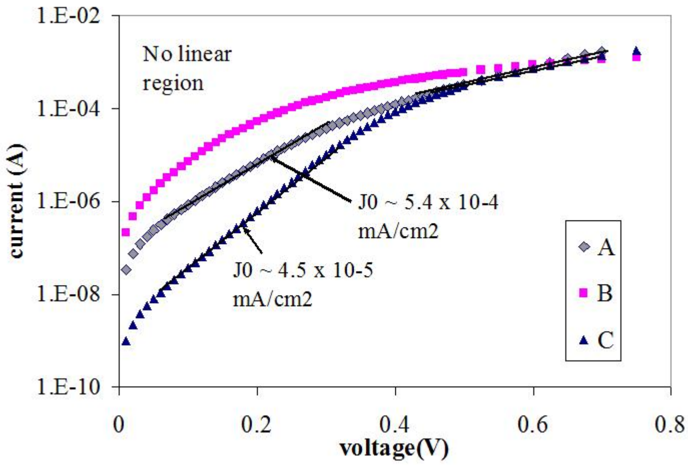

Figure 4.4 dark I-V characteristics of nc-(Si,Ge) device

CHAPTER 5. TRANSPORT PROPERTIES

In this chapter I explain the experimental setup and the measurement procedures used in lifetime measurement. We will first discuss the theory which governs this technique.

5.1 Lifetime measurement

5.1.1 Theory of reverse recovery(R.R) technique

Though it is not clear from literature who developed R.R method originally, but it was Kingston et.al who gave quantized this theory and derived an equation for minority carrier lifetime through the R.R phenomena. Later Lax et.al gave a comprehensive proof of that equation, which is again shown below.

$$erf\left(\sqrt{\frac{T_{rr}}{\tau}}\right) = \frac{I_f}{I_f + I_r} \tag{5.1}$$

In this experiment we examine the variation of a $p-n$ junction voltage when it is switched from forward to reverse bias. In a forward biased $p-n$ junction, which in our case would be a p^+-n junction, the hole concentration is governed by the equation

$$\frac{\partial p}{\partial t} = D\frac{\partial^2 p}{\partial x^2} + \frac{p_n - p}{\tau} \tag{5.2}$$

The total forward current can be approximated to the diffusion current given by

$$I = -qDA\frac{\partial p}{\partial x}|_{x=0} \tag{5.3}$$

$$p_0 = p_n exp\frac{qV_j}{KT} \tag{5.4}$$

The excess hole concentration(Δp) in the n-layer during the forward bias is given by

$$\Delta p = \Delta p|_{x=0} exp^{\frac{-x}{L_p}} \tag{5.5}$$

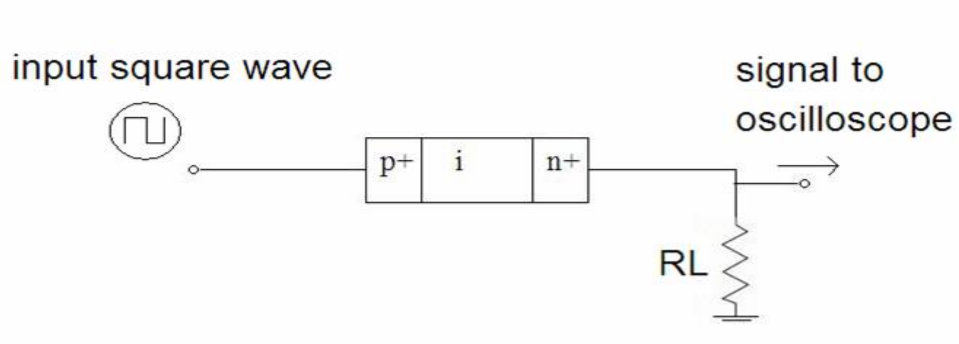

Figure 5.1 schematic of the circuit used for lifetime measurement

where L_p is the diffusion length of the holes. When the applied voltage is reversed voltage the junction should satisfy the equation and the current through diode is governed by

$$V = V_j + IR \tag{5.6}$$

Solving the above set of equations gives us the junction voltage,

$$V_j = \frac{kT}{q} log_e \left(1 + \frac{I_f}{I_s} - \frac{I_f + I_r}{I_s} erf\sqrt{r}\right) \tag{5.7}$$

Substituting V_j=0 in the above equation gives us the lifetime equation mentioned before (equation 5.1).

The key observation here is that it is assumed throughout this derivation that current is governed by diffusion and the voltage across the diode within the storage delay time remains constant. Though these two assumptions look independent, we later show they are actually interdependent and this assumption is invalid in some of the solar cell structures we experiment with.

5.1.2 Experimental Setup

Figure 5.1 shows the simple circuit used in the lifetime measurement setup. We have the DUT (device under test) connected in series with a resistor. Two different setups have been used one for room temperature measurements and second for high temperature measurements, both of which are explained separately here. In either setup, a square waveform is applied using

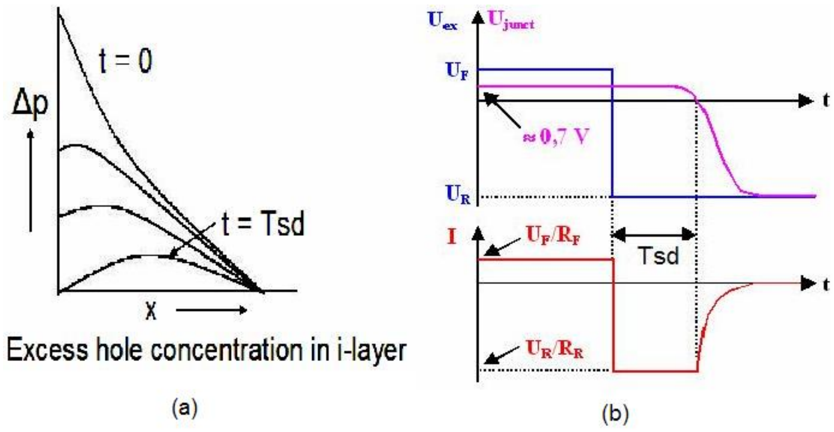

Figure 5.2 (a)Distribution of excess carrier concentration in the base layer at various times from t=0 to t=T_{sd} (b)The current and voltage waveforms(voltage across diode shown in pink, external applied voltage shown in blue)

a Agilent 33220A 20MHz function / arbitrage waveform generator on the positive terminal (p side of a p-n device). The voltage across the load resistor is sensed in Tektronix TDS3052 500MHz, 5Gs/s digital oscilloscope.

Though room temperature setup was built first, when high temperature measurements were needed, we had to move to a different setup. We initially planned to have a silicone heater inside the existing box. Later, to save time and effort, we decided to use the existing SCLC setup which has a heater setup already. High temperature setup: The sample is placed on a small aluminum heater block, which itself is placed in a bigger aluminum box. The BNC cable carrying the input voltage waveform is connected to one of the two BNC adapters on the box. The back contact of the device is connected to the second BNC adapter through a co-axial cable, which is terminated outside onto a Pomona 50Ohm BNC in-series attenuator. The voltage on this attenuator is sensed using a 10x probe in the oscilloscope. The Aluminum block is heater using a 120 Volts heater connected through a cable to the bottom of the heater which of placed outside the box. With this setup temperatures from 23C to 190C could be realized. The thermocouple wire is placed beside the sample. Room temperature setup: The setup is enclosed in a metal box. The sample is a placed on a PCB board coated with copper on both sides. The copper on the top side of the PCB is stripped off everywhere but on a small area big to allow room for the sample to sit on. An SMA jack is soldered to the top copper side onto an edge of the PCB. The bottom two ground poles of this SMA jack are soldered to the bottom copper side of the PCB, which actually serves as a common ground for the whole system. The same ground is also connected to the ground of the BNC adapters on the surface of the box through a copper metal piece soldered to the bottom of the PCB. The board is screwed on to the platform provided on the sides of box. Signal from the input BNC adapter is passes through an SMA cable which is in turn connected to a gold needle probe through a Pyrex glass cube. This probe piece sits on the PCB itself on the area where we have the copper stripped. Note that in our setup the steel substrate is shorted to the top side of the PCB which is in turn connected to the SMA jack. Therefore the current through the DUT passes through the SMA jack to the load resistor which is connected to one of the BNC adapters outside the box. Both the above discussed setups are represented in Figure 5.3

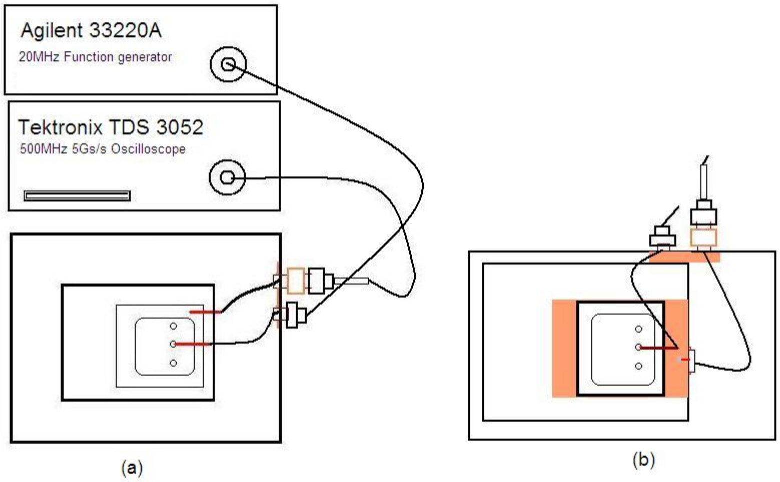

Figure 5.3 Experimental setups used for lifetime measurement (a)Setup built in an Aluminum box (b)Setup where PCB board is used as a common ground

During the course of several measurements I came across several problems related to the experimental setup, which can be avoided if one is careful with various probes and the instruments. So below are some guide lines which can be used to avoid errors:

- Since we are dealing with nanosecond rise time-waveforms, having a good common ground is very important. It is suggested that the ground plane has as large area as possible. Also, the ground shield of the both the probe wires (SMA cable and normal electric wires) can be grounded to reduce some of the ringing seen in the reverse recovery waveforms. Most of the cables were minimized in length.

- Surprisingly it was found that the settings of oscilloscope, if set inappropriately can give rise to wrong waveforms i.e., waveforms with erroneous rise/fall times which means the oscilloscope is acting as filter or waveforms with voltage spikes on the rise/fall edges. The relevant settings can be FFT algorithm, interpolation method and bandwidth.
- Proper compensation of the 10x probe is also important to ensure that frequency response of the probe/scope is flat within the bandwidth limits of the scope and probe. An example of a poor reverse recovery waveform is shown in Figure 5.4.
- In case of the room temperature setup, sometimes the back of the sample had to be sanded to remove oxide and ensure a good contact. A bad contact in this case can also give rise to voltage spike as shown in Figure 5.4.

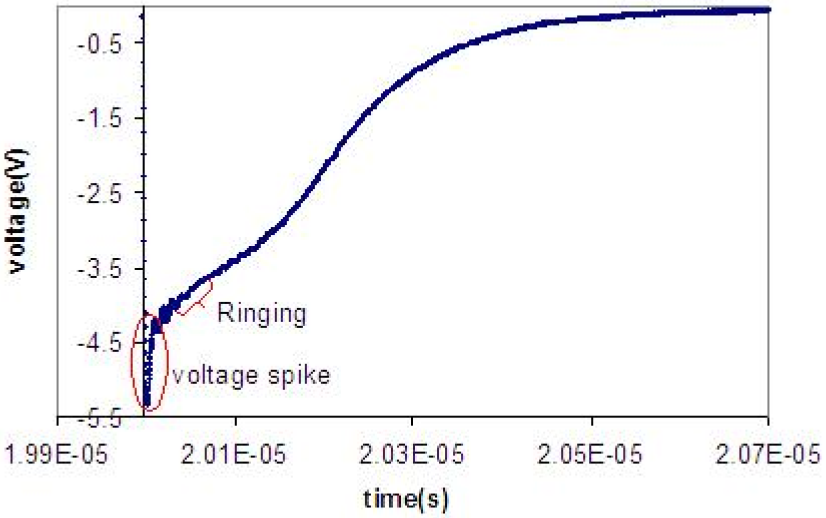

Figure 5.4 Reverse recovery waveform demonstrating ringing in the circuit

- To ensure that the probe setup is good, frequently I did calibration measurement by sensing a square waveform from a function generator terminated on to a 50Ohm resistor using the 10X probe.

5.1.2.1 Measurement procedure

The following guidelines explain the whole calculation method in various steps:

1. As mentioned in section , the lifetime experiment consists of the calculating Trr for various If, Ir. So we need to collect the reverse recovery waveforms for various If and Ir values. So adjust the If and Ir values to get a good waveform.
2. Set the oscilloscope to ”average” mode from the default ”sample” mode and select the number of cycles to be 512 to make the waveform smoother. Once the averaging is done the run/stop light goes off, which means we can now save the waveform on to the floppy. Six such waveforms can be saved on to one floppy. Make sure you are saving the waveforms in .CSV format which is readable through Excel
3. The plot of the .CSV file in excel will reproduce the reverse recovery waveform from which we need to calculate Trr. We need to identify the linear region of voltage drop followed by semi-exponential drop. The latter part often looks like a linear drop itself since the time is varied only over small range of values. Once the two straight lines are fit in Excel you can easily how long the initial flat part lasts and that gives Trr. Also note down If, Ir values.
4. There was a excel template made to actually plot the Trr versus the square of inverse error function. The inverse error cannot be directly computed in excel and hence Matlab was used for this purpose.
5. Incase of temperature measurements, the sample was always soaked at a new temperature for at least 15mins to ensure it as reached the new temperature. Since we the samples are often placed on a glass slide there can be finite difference between the thermocouple temperature and the actual device temperature.

5.1.2.2 Calibration of the setup

To verify that setup was giving correct measurements and also check that our method of calculation was correct, a calibration measurement was done on n+-p diode fabricated on a p type wafer. Lifetime of the minority carriers (electrons) and diffusion length were measured using reverse recovery and Q.E techniques respectively. Mobility was then deduced from these values and verified with the value calculated from the doping of the wafer provided by the manufacturer. Diffusion length calculation is shown in Figure5.5 and the equation used is

$$Q.E = \frac{\alpha l}{1 + \alpha l} \Rightarrow \frac{1}{Q.E} - 1 = \frac{1}{L}.\frac{1}{\alpha} \tag{5.8}$$

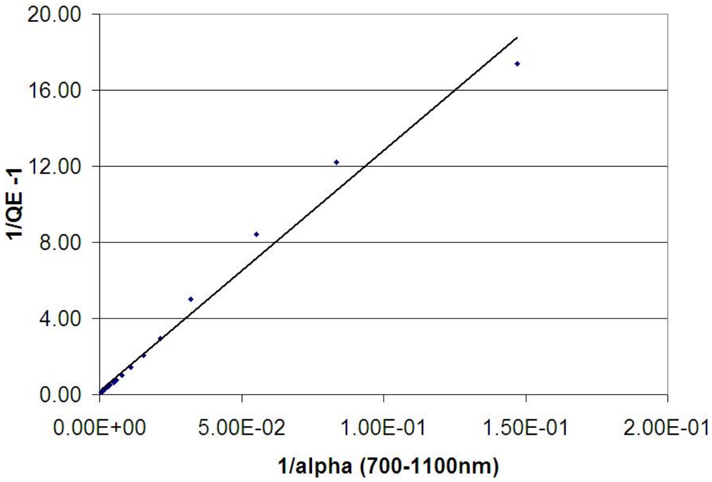

Figure 5.5 Diffusion length measurement in c-Si

Note that one needs to measure absolute Q.E for the diffusion length calculation and the wavelength range used is 700 - 1100nm. This measurement was measured on ITO contact and hence the reflectivity of ITO at various wavelengths was taken into account while deducing 'α' in the above equation.

Also several measurements were done on commercial diodes. Figures 5.6 show the reverse recovery waveforms on a slow and fast diodes.

Table 5.1 Comparison of calculated mobility from lifetime experiment with theoretical value

Experimental values	Calculated mobility $\mu = \frac{q}{KT} \cdot \frac{L^2}{\tau}$	Theoretical Mobility
Diffusion length(L) 77μm Lifetime(τ) 1.87 μs	1268$\frac{cm^2}{Vs}$	1100$\frac{cm^2}{Vs}$

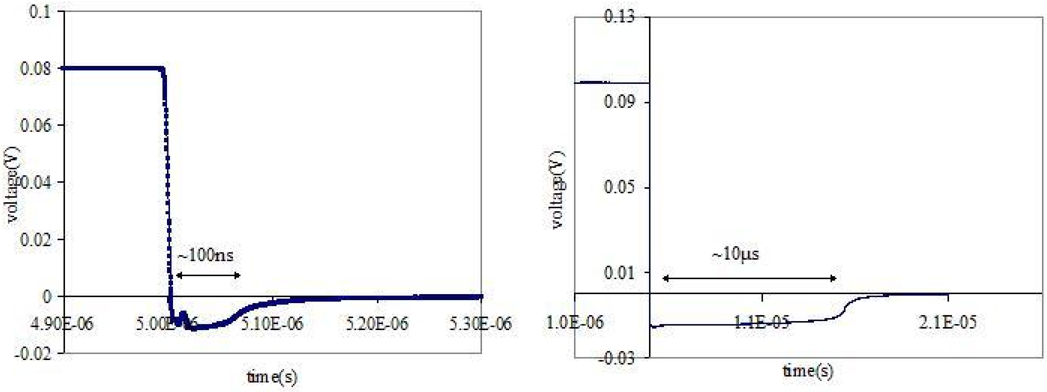

(a)

(b)

Figure 5.6 Reverse recovery waveforms in a (a)fast diode, (b) slow diode

5.2 Measurements in nc-Si and nc-(Si,Ge)

Lifetime measurements have been performed on several nanocrystalline devices. Figure 5.7 shows the reverse recovery waveform collected on a nc-Si device. The square voltage waveform used here has the following parameters: V+ = 4.0V, V- = 3.8V. Note that before t=0, the voltage across the resistance is 3.5V which indicated the positive bias on the device is 0.5V assuming there is no voltage drop along the wires. Also the negative voltage across the resistance is 4.2V which is nothing but the sum of V- (of square wave) and positive bias of the device. This matches well with our understanding of the reverse recovery theory.

Several such waveforms were collected and the corresponding If, Ir and Tsd are noted for each waveform. To obtain consistency among calculations, we kept If constant within each plot and varied Ir. Note that there is range of Ir values we can use for each sample. If Ir is too high the storage time would be negligible and if it is too low, the storage delay time will tend to merge into the exponential decay part. In each case to calculate the duration of storage delay time,

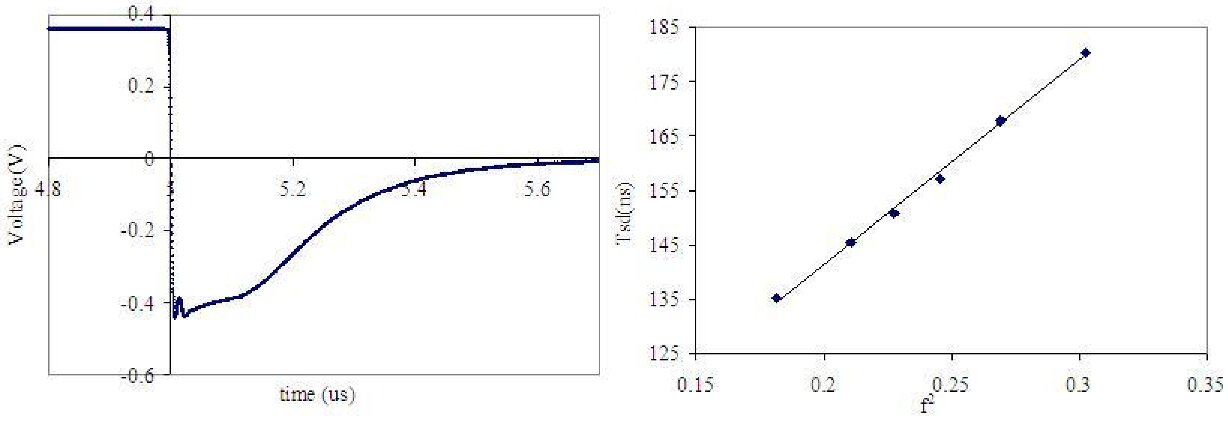

(a)

(b)

Figure 5.7 (a)Reverse recovery waveform in a nc-Si:H device (b)Straight line fit for the T_{ds} Vs f^2 data

two straight lines were fit, one within the storage delay time and the other in the initial part of exponential drop, which is approximately linear. The corresponding straight line fit is shown in Figure 5.7. A similar experiment on a nc-(Si,Ge):H device is demonstrated in Figure 5.8.

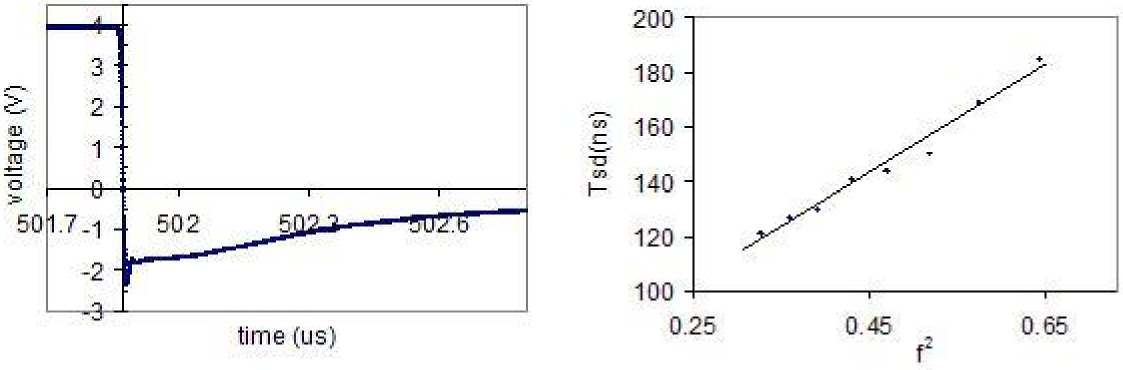

(a)

(b)

Figure 5.8 (a)Reverse recovery waveform in a nc-(Si,Ge):H device (b)Straight line fit for the T_{ds} Vs f^2 data

Figure 5.9 compares the typical lifetimes measured in nc-Si and nc-SiGe materials. The average lifetime in nc-Si is 400ns and that of nc-SiGe is 250ns.

Some of the non-ideal effects seen while performing these calculations are listed below:

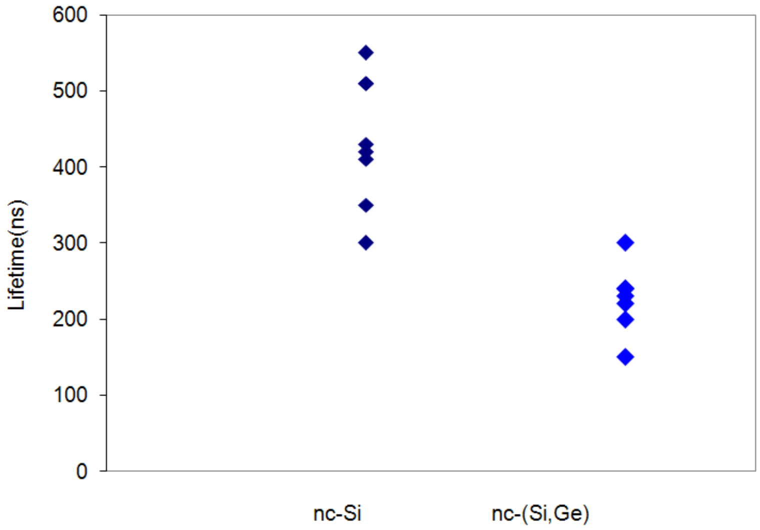

Figure 5.9 Comparison of lifetimes calculated in nc-Si and nc-SiGe devices

- Normally the bias across the device was observed to reduce by 0.1-0.2V immediately after application of reverse bias
- The straight line fit of the storage delay times should pass through origin, but in our experiments we always observed a positive y-intercept, including the experiments done on crystalline silicon. But it was observed that most of the cases the y-intercept was close to 0.1-0.2 times the storage delay times and was hence neglected. A higher y-intercept was taken as an indication of some experimental error.
- As mentioned before I_f was kept constant in each calculation. When measurements were repeated for different I_f values variations of 6% were observed.

Table 5.2 Lifetime calculation for different forward currents

$I_f(mA)$	$\tau(ns)$
90	518
82.5	501
75	555
65	567

5.2.1 How device structure affects the reverse recovery waveforms?

When we compare Figures 5.7 and 5.6, it is very clear that the bias across the DUT remains constant in case of the commercial diode but not in the case of a nc-Si device. The bias across the device decreases slightly within the storage delay part incase of the nc-Si devices. The reason for this can be explained by taking a closer look at the assumptions behind the lifetime. Lax et al reported the first derivation of the lifetime equation. They assume a purely diffusion controlled transport and assume that the junction voltage remains constant in storage delay part. In our nc-Si devices we always have a small electric field present in the intrinsic layer. To fabricate a $p^+ - n - n^+$ device the procedure we use is as follows. First deposit n+ in a VHF PECVD reactor (R2) and then transfer to another VHF reactor (R1) used for intrinsic layer depositions. For p^+ layer the device is again transferred back to the first VHF reactor (R2). So when we first start depositing base layer in R1, there is some remnant oxygen in the chamber which might make the base layer slightly n-type initially, but as the deposition proceed the base layer becomes less n-type. So we have an inherent graded doping which can give rise to a built-in electric field. This in turn gives rise to a small voltage drop in the storage delay part of the reverse recovery waveform. To prove that the above reasoning is correct, devices were fabricated with significant built-in electric field by having graded TMB doping in the base layer. The band diagram of the base layer in this case is shown in Figure 5.10. The excess holes would just drift away in the presence of this electric field as opposed to recombination at rate of their lifetime. Another important feature of the recovery waveform is the linear voltage drop (for most of the duration).

Comparison with the time of flight (T.O.F) experiment:

The above case of drift controlled recovery can be understood better when we compare it to the T.O.F experiment. The typical experimental setup for T.O.F measurement and its current waveform are shown in Figure 5.11. In a T.O.F setup we shine light (essentially generate excess carriers) on one end of the sample, across which we also have a constant DC voltage

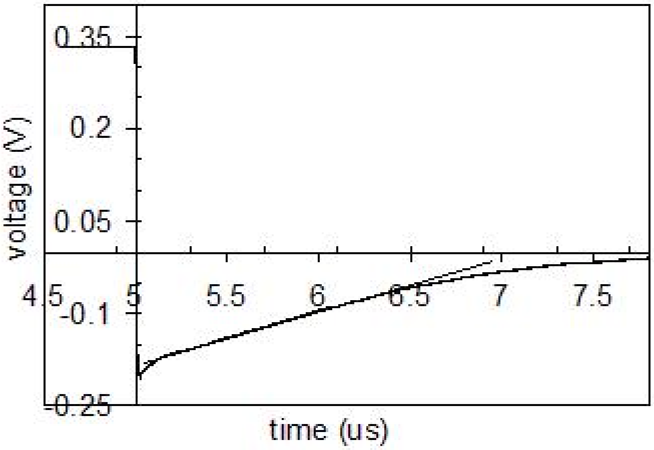

Figure 5.10 Reverse recovery waveform showing no flat part demonstrates the presence of strong electric field in the base layer

applied. The generated excess carriers then drift to the other end of the sample and in this process they also recombine. If we measure the transient current through the sample during the times when the excess carriers are entering (being generated) or leaving the sample we see a linear change in current. The linear decrease when the excess carriers are exiting the sample can be compared to linear decrease of current in the reverse recovery waveform in the case of high electric field in the base layer.

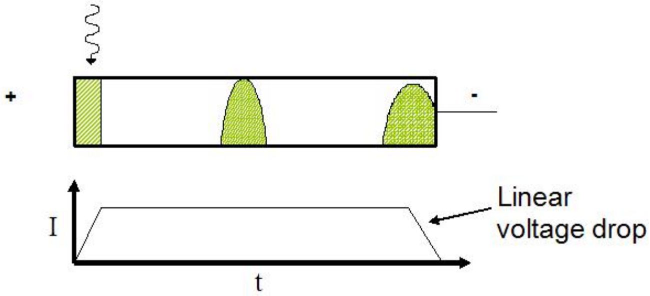

Figure 5.11 Drift and diffusion of excess carrier concentration in a T.O.F experiment and the corresponding current waveform

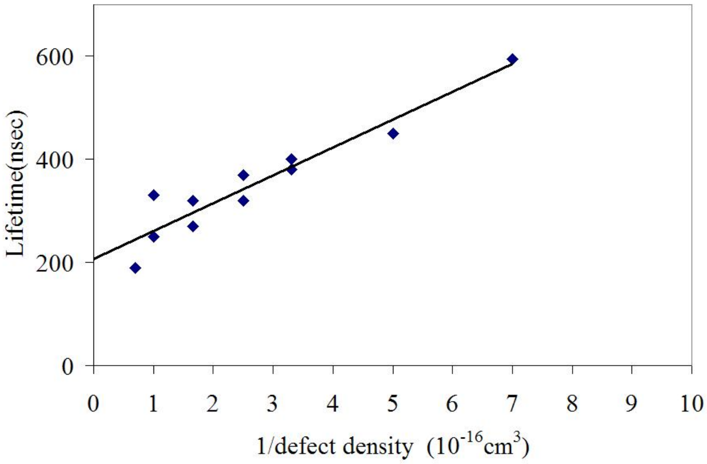

Figure 5.12 Straight line fit of minority carrier lifetime Vs inverse of defect density validating S.R.H recombination theory

5.3 Variation of lifetime with defect density

This section reports the most important set of experiments in this work: to prove that the lifetimes we are measuring obey SRH model. The following equation gives the lifetime of a minority carrier assuming the SRH model of recombination holds true.

$$\tau_p = \frac{1}{\sigma_p \upsilon_t h N_T} \tag{5.9}$$

Minority carrier lifetimes and defect densities are measured in the same nc-Si devices and a plot of lifetime versus inverse of defect density $(1/N_D)$ is plotted in Figure 5.12. The straight line fit we obtained matches with what we expect from equation5.9. Defect densities were measured from C-V techniques as explained in a previous section. Also from the slope of the straight line we could get an estimate of the capture cross section of defects for holes The value obtained for as 2x$10^{-16}cm^2$, matching well with the value found from literature.

Lifetime versus defect density in nc-SiGe

Figure 5.13 shows lifetime measured versus defect density in nc-SiGe devices. Higher defect densities do lead to lower lifetimes. The defect densities could only be varied from $5*10^{15}cm^{-3}$ to $5*10^{16}cm^{-3}$. Hence the variation on x-axis of this curve is less compared to Figure 5.12. As an approximation we can fit a straight line to this data and conclude that SRH model of recombination holds true. Note that this curves contains data from devices with various germanium contents and devices made with variable ppm TMB doping. The least defect density achieved was $610^{15} cm^{-3}$.

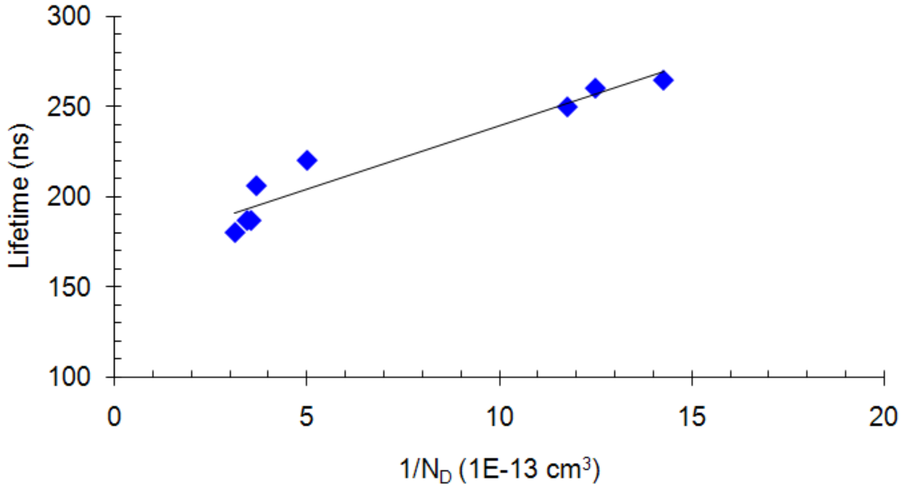

Figure 5.13 Lifetime versus inverse of defect densities, verifying SRH model of recombination in nc-SiGe

5.4 Variation of lifetime with temperature

The effect of temperature on any recombination mechanism reveals important information about the fundamental process through by which the recombination takes place. Hole lifetime versus temperature was an important study we performed. Lifetimes were measured from the range of 25°C to 200°C.

How Oxygen doping reduces Lifetime

The Oxygen contamination from the reactor makes the base layers slightly n-type by default. The electrons released by the Oxygen atoms, fill up the trap levels, primarily located at the grain boundaries. The traps can now act as recombination centers and hence reduce the hole lifetime or diffusion length.

Method of measurement

The sample was placed on a glass slide on the heater-aluminum block. Since the thermocouple is attached to the aluminum block, the actual sample temperature might be 10-20C lesser than the indicated temperature. The measurements were recorded at smaller temperature intervals like 15-20C to avoid any artifacts and the detrimental effects of inherent error bars. The samples were soaked at each temperature for about 15mins to make sure error in the temperature is minimized. Also the measurements were taken starting from the maximum temperature and cooling it down. It was expected that the delta between the actual and indicated temperatures could be reduced by adopting a procedure like this.

Result

Two distinct regions were found in the lifetime versus temperature graphs, consistently in all the nc-Si samples. The lifetime decreases from 500ns to 250ns from 25°C to 100°C and increases back to the range of 500ns when temperature is further increased to 200°C. This behavior can be explained based of the SRH mechanism. Assuming that there is a distribution of trap levels in the band gap of the nc-Si, there are two competing processes taking place which determine the possibility of recombination of a minority carrier (hole) at a particular trap level viz., electron escaping back to conduction band from trap and hole being captured into the trap.

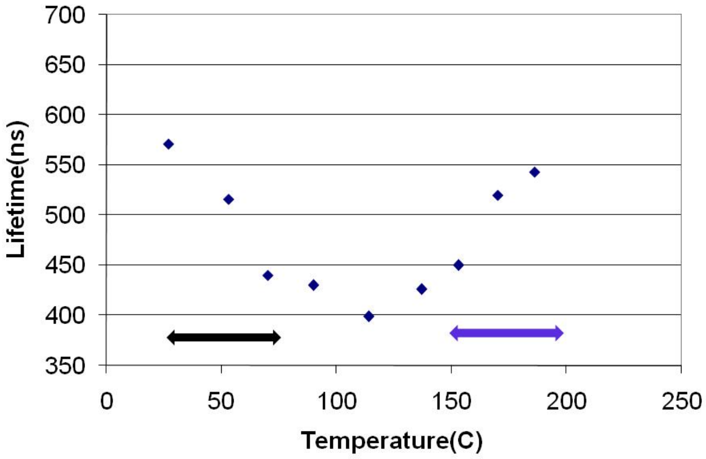

Figure 5.14 Variation of Lifetime with temperature in a nc-Si device

Quantitative analysis

The presence of a majority carrier (electron in our case) at the trap level is controlled primarily by the temperature i.e., the thermal excitation of electrons back to the conduction band after being trapped. At lower temperatures (25°C-100°C), the probability of electrons exciting back to conduction band is less and hence hole recombination is controlled only by the trapping of holes, which increases with temperature because of more thermal collisions. When the temperatures are high enough that the electrons start to excite back to conduction band the trap level fails to act as a recombination center. Therefore lifetime begins to increase for temperature beyond 100°C.

Qualitative analysis

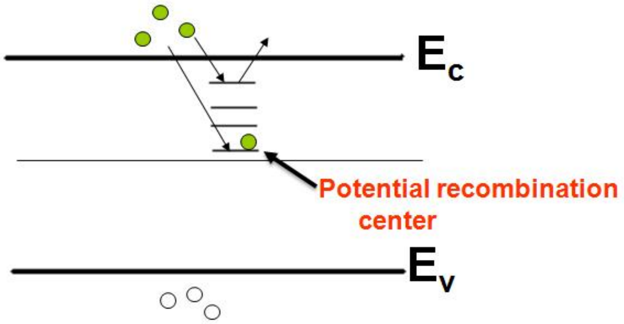

Figure 5.15 Energy band diagram showing that only deep defects remain filled with electrons

The decrease of lifetime in the initial part of the lifetime versus temperature curve can be explained from the SRH equation. As thermal velocity increases collisions among the holes increases and they tend to recombine more.

$$\tau_p = \frac{1}{\sigma_p v_{th} N_T} \tag{5.10}$$

To quantitatively explain the second part of the lifetime curve, we plot the values of the escape frequency of electrons and capture frequency of holes for a trap level at Ec-Et = 0.35eV. Since the capture frequency varies as $1/\tau$ and lifetime does not change by orders, capture frequency seems to remain constant on a log scale and lies in the range of 2E6s^{-1}. But the escape frequency of electron give by the formula, changes by orders of magnitude because of the logarithmic dependence on temperature.

$$\upsilon = \upsilon_0 exp^{\frac{-(E_C-E)}{KT}} \tag{5.11}$$

From the figure5.16, we can see that the escape frequency increases from the range of 1E4s^{-1} at room temperature to 1E7s^{-1} at 200°C. So, around temperatures of 100°C the escape frequency of electron becomes more than the capture frequency and lifetime begins to increase.

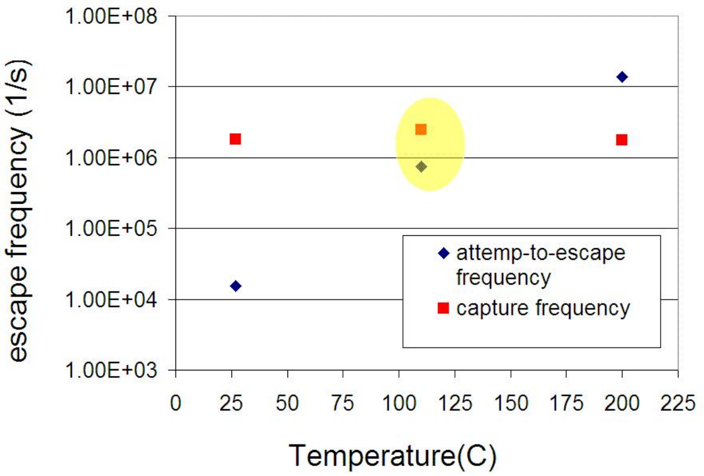

Figure 5.16 Variation of hole capture frequency and electron escape frequency with temperature

Lifetime versus temperature in nc-SiGe

Similar measurements in nc-SiGe were also measured. The plot is shown in Figure 5.17. The RR curves taken at temperatures more than 75C, because at lower temperatures the flat part of RR waveform was not clear enough and the calculations were considered unreliable. Beyond 110C we see that lifetime increases marginally. One possible explanation for this would be that deep defect density is much more than the shallow defects. In such a case, increase of temperature will make the shallow defects not effective for recombination and that will not effect the lifetime much. According to this explanation, if we go to further high temperatures we should see a higher rate of increase of lifetime. But that was not studied, because beyond 200°C, the device structure might start to change like Boron diffusion.

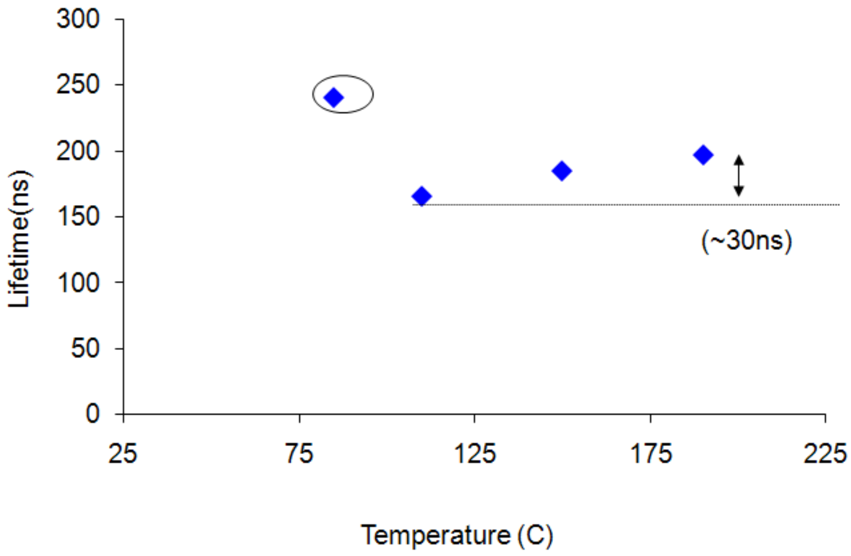

Figure 5.17 Lifetime versus temperature in nc-SiGe device

5.5 Capacitance versus frequency

The study of capacitance versus voltage at various freuqencies gives us useful insight about the distribution of trap levels in nc-Si and nc-SiGe, which will be discussed in this section.

Measurements in nc-Si

Figure 5.18 shows C-V curves taken at various frequencies from 120Hz to 100KHz.We note that at higher frequencies (100 KHz) the capacitance saturates at 19.5nF/cm^2. The depletion width corresponding to this value is 0.54μm, the same can also be confirmed from the reflection measurements. The frequency at which the curves start to change from two line curve to the saturation kind of curve indicated the location of traps, which has been calculated to be 0.35-0.5eV below conduction band [10].

Measurements in nc-SiGe

Figure 5.19 shows the data taken from a nc-SiGe device. The overall behavior is similar in this case, but we can notice that as we increase the frequency from 10KHz to 100KHz the amount of decrease of capacitance is much more than the case of nc-Si. Beyond 100KHz the capacitance decreases only marginally. This can also be interpreted as a high trap density compared to

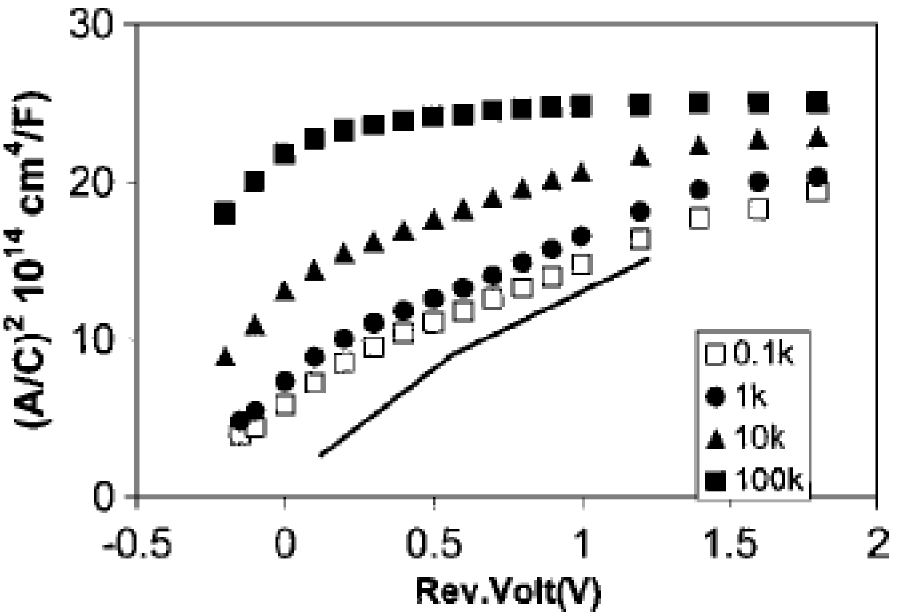

Figure 5.18 C-V curves at various frequencies form 120Kz to 100KHz in a nc-Si device[10]

shallow defects. As we increase frequency from 10KHz to 100KHz we are eliminating the trap states slightly above mid gap states.

5.6 Measurement of Diffusion length

The typical values of diffusion lengths measured in nc-Si devices, using the reverse bias Q.E method, are in the range of 0.5 -3μm. This method has also been reported in [10]. It is interesting to note that nc-(Si,Ge):H devices also showed diffusion lengths of the order of 0.1-2μm, matching very well with values normally seen in nc-Si:H. The value of the diffusion length is one of the key reasons why a nc-Si based solar cell cannot be made too thick, since the collection of carriers will be limited by diffusion length in thick devices.

Particularly in nc-SiGe, it was found that as we increase the germane content the calculated diffusion length decreases as shown in Figure 5.20. In these devices, the silane gas flow was reduced keeping the 10

As discussed in previous sections, at higher germane contents, there is a degradation in the

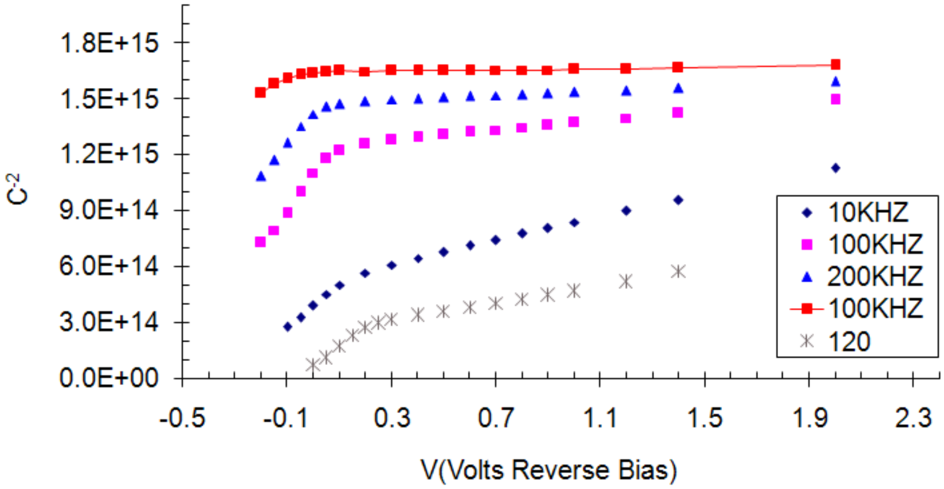

Figure 5.19 C-V curves plotted at various frequencies, collected on a nc-SiGe device.

crystallinity of the nc-SiGe film. This can be interpreted as insufficient passivation of dangling bonds at the grain boundaries. In this particular case we have three different crystallites growing simultaneously.

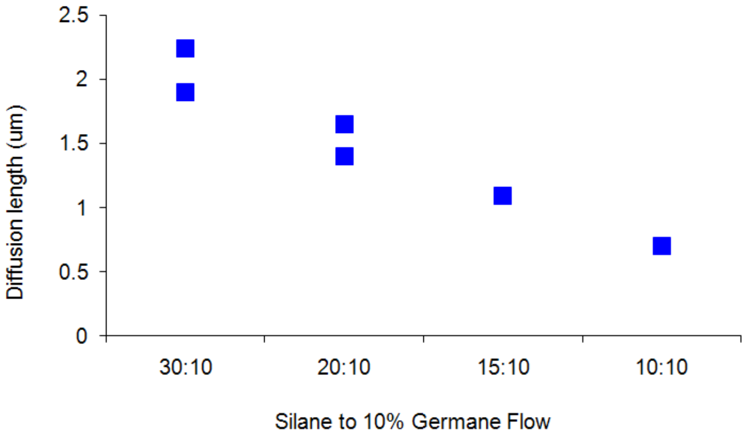

Figure 5.20 Diffusion length versus germane content in the device

5.6.1 How to improve diffusion length of holes?

Recombination in nc-Si happens mainly through defect states (SRH model). We can achieve a high diffusion lengths or lifetimes in this material by minimizing the presence of defects states. Another way enhancing the transport of minority carrier is to have a field assisted transport. To enhance the collection of holes in the base layer of a solar cell device, we have adopted graded TMB doping technique which can provide an internal electric field driving the holes towards the p^+ contact. The band diagram of the base layer with electric field and the corresponding diffusion length calculation are shown in Figure5.21.

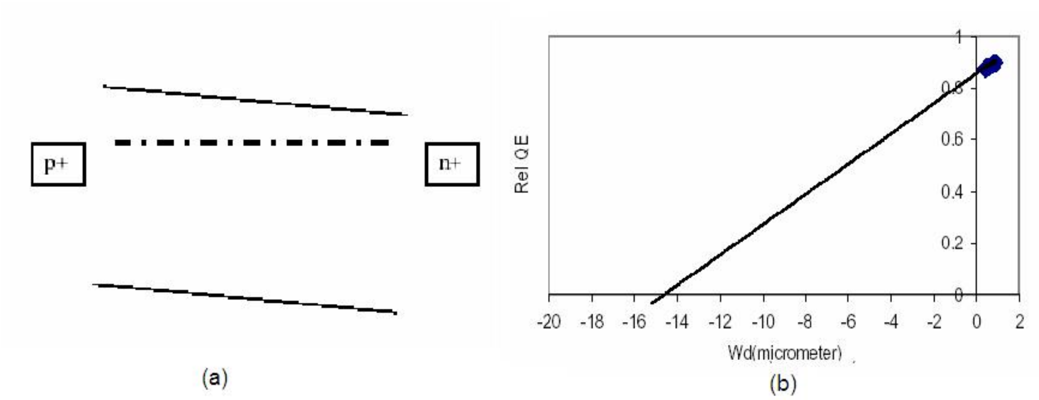

Figure 5.21 (a) Internal Electric field developed from the graded TMB doping (b) Plot showing enhanced diffusion length of holes in nc-Si:H

5.7 Calculation of Mobility

Mobility can be calculated from lifetime and diffusion length data sing the relations

$$\frac{D}{\mu} = \frac{kT}{q} \qquad L^2 = D.\tau \tag{5.12}$$

The values obtained in nc-Si:H were in the range of the 1-2 $cm^2(Vs)^{-1}$. This can be considered as a confirmation that our measurement of lifetime and diffusion length are correct and the value also matched well the literature[83, 84].

We could also get an estimate of the mobilities in nc-(Si,Ge):H. Since the lifetimes in nc-

(Si,Ge):H were generally 0.5 to 0.75 times that of nc-Si:H, (the variation coming from the variable amounts of Germanium present in different samples, which we have not quantized), and the diffusion lengths are essentially same as that of nc-Si:H, the lifetimes are 1.33 to 2 times that of nc-Si:H. Therefore we can estimate the mobilities in nc-(Si,Ge):H to be 1-4$cm^2(Vs)^{-1}$.

CHAPTER 6. SUMMARY AND FUTURE WORK

In this chapter the results obtained in this work are summarized followed by a discussion of the ideas for future work.

6.1 Conclusion

- We successfully measured various transport properties (diffusion length, mobility, capture cross-section, defect densities)in the same device. Consistent results have been obtained from various experiments.

- For the first time we showed that ”Reverse recovery technique” works well in nc-Si:H and in nc-(SiGe):H materials. Lifetime data complies with SRH model, verified from lifetime versus defect density measurement. The fact that this model based on crystalline material has been applied to these nanocrystalline materials indicates that these materials have high degree of crystallinity.

- The lifetime values obtained in nc-Si device were in the expected range(300-600ns). The lower values of lifetime observed in nc-SiGe(150-300ns) are an indication of the poor transport properties which can arise from the dangling bonds at the grain boundaries. This problem is particularly sever in nc-SiGe because we have three different types of crystallites grown simultaneously.

- The current densities in SiGe devices were comparable to nc-Si devices, for lesser device thickness than that of the latter. This is an indicative of the higher absorption coefficient in nc-SiGe. We can reduce the bandgap of the material depending on the amount of Ge incorporated. Similar effect of also observed when we compare Q.E data of two devices of nc-Si and nc-SiGe of same thickness. We can clearly see that we have enhanced absorption in the infrared regime in the case of nc-SiGe.

- It was also observed that the reverse recovery method of lifetime calculation is limited only for diffusion controlled transport. In device with microdoping technique, we cannot implement this technique.
- We proved that enhanced collection of holes can be achieved by creating an internal electric field by doping with ppm level of Boron. This has resulted in improvement of diffusion length of holes in nc-Si:H with value increasing from $1\mu m$ to $10\mu m$. In nc-SiGe we obtained only marginal improvements from 0.5μm to 2.5μm. Since we have electric field what we measure in this case can be termed as range, this parameter still gives a good estimate of how good the transport is taking place in the device.
- By measuring lifetime versus temperature, we could estimate the location of the trap levels to be 0.4-0.45eV below conduction band in nc-Si, which is an important parameter that can be used in modeling devices.
- The mobility values calculated from the measured diffusion length and lifetime turned out to be in the correct range of 1-2cm^2/Vs for nc-Si. In nc-SiGe, estimated mobility is >1cm^2/Vs because of the lower lifetimes and comparable diffusion lengths.

6.2 Future work

- We have observed that presence of a strong electric field renders the R.R method ineffective for measuring lifetime. Therefore we need to model the reverse recovery equation to include the effect of electric field, for which we can possibly assume a constant electric field $\overrightarrow{E}$ throughout the base layer and solve for the junction voltage. A preliminary calculation is shown below:

$$\begin{aligned}\frac{\partial p(x,t)}{\partial t} &= -\tfrac{1}{q}\tfrac{\partial J_p}{\partial x} - \frac{\delta p}{\tau_p}\\ \frac{\partial p(x,t)}{\partial t} &= -\mu_p E\tfrac{\partial p(x,t)}{\partial x} + \tfrac{D_p}{q}\tfrac{\partial^2 p(x,t)}{\partial x^2} - \frac{\delta p}{\tau_p}\end{aligned}$$

Here we assume that we have a constant electric field, but still account for both diffusion and drift components of the current. Also we can assume that the junction voltage drops from V_f to 0 at the end of the reverse recover period falling in a linear fashion:

$$V_j = V_f\left(1 - \frac{t}{T_{rr}}\right) \tag{6.1}$$

The resulting solution for the junction voltage will be,

$$I_s[e^{\frac{qV_j(r)}{KT}} - 1] - I_f\left(1 - erf\sqrt{r}\right) - I_R.erf\sqrt{r} =$$
$$\frac{-1}{R\sqrt{\pi}}\int_0^r \frac{e^{-(r-s)}.V_J(s)}{\sqrt{(r-s)}}ds - \frac{\gamma}{\sqrt{\pi}}\int_0^r \frac{e^{-(r-s)}e^{\frac{qV_J(s)}{KT}}}{\sqrt{r-s}}ds$$

where V_J(t) is the junction voltage during the storage delay duration, r and s are parameters defined as r=τ/Trr, s=t/Trr, I_R is the reverse current defined as V_R/R, I_f is the forward current, I_f=$I_sqA\sqrt{D}p_n/\sqrt{\tau}$. This procedure has been taken from [85]. The solution of the above equation is parameter r, which gives lifetime τ. The above equation needs to be simplified further to be applicable for lifetime experiments. Also, a more detailed calculation can be done without assuming a constant electric field.

- Further experiments need to be performed on nc-(Si,Ge), to understand the crystal growth of this material. From Raman studies, it was found that obtaining good crystallinity in all the three types of crystallites in this material would be a difficult task. Amount of hydrogen dilution needed for Ge crystallization is much more than Si, which means Si-Si crystals might be too crystalline at that hydrogen dilution. Reducing the overall amorphous content of the film can improve the transport properties.

- SCLC measurements can be carried out in nc-(Si,Ge):H material to check whether incorporation of Ge is in fact resulting in mobility enhancement. No prior reports of mobility measurement in nc-(Si,Ge):H in device structures have been found in literature. SCLC technique in device structures has already been implemented in nc-Si [83].

- If we have characterized methods for diffusion length and lifetime measurements, we can incorporate these parameters in the standard solar cell model.

BIBLIOGRAPHY

[1] http: *//en.wikipedia.org/wiki/Greenhouse.gas*

[2] *http* : *//en.wikipedia.org/wiki/Kyoto.Protocol*

[3] http: *//www.msnbc.msn.com/id/*12400801

[4] Martin A Green, Chap.4. Crystalline silicon solar cells.

[5] http: *//www.solarbuzz.com/StatsCosts.htm*

[6] Martin A Green, J Mater Sci: Mater Electron (2007) 18:S15S19

[7] Y.Hamakawa, Thin-Film Solar Cells, Springer, 2004

[8] Alan L.Fahrenbruch, Richard H.Bube, Fundamentals of Solar cells, Academic Press Inc, 1983

[9] Jenny Nelson, The Physics of solar cells, Imperial College Press, 2003

[10] VL Dalal, P Sharma, *Applied Physics Letters* 86 (2005) 103510

[11] Kenji Yamamoto, Masashi Yoshimi, Yuko Tawada, Susumu Fukuda, Toru Sawada, Tomomi Meguro, Hiroki Takata, Takashi Suezaki, Yohei Koi, Katsuhiko Hayashi *Solar Energy Mater. And Solar Cells* 74 (2002) 449

[12] A. V. Shah, J. Meier, E. Vallat-Sauvain, N. Wyrsch, U. Kroll, C. Droz and U. Graf, *Solar Energy Mater. And Solar cells* 78 (2003) 469

[13] B. Rech, O. Kluth, T. Repmann, T. Roschek, J. Springer, J. Mller, F. Finger, H. Stiebig and H. Wagner, *Solar Energy Mater. And Solar Cells* 74 (2002) 439

[14] Debju Ghosh, R. Shinar, J. Shinar and V. L. Dalal, *Proc. Mat. Res. Soc. Symp.* 989 (2007) A12-01

[15] Debju Ghosh, R. Shinar, J. Shinar and V. L. Dalal, *J. Non-Cryst. Solids* 2007

[16] Durga Panda and Vikram Dalal,*Proc. Mat. Res. Soc. Symp.* 910 (2006) 615

[17] C. H. Lee, A. Sazonov, A. Nathan and J. Robertson, *Appl. Phys. Lett.* 89 (2006) 252101

[18] S.Veprek, V.Marecek, *Solid State Electronics* 11 (1968) 683

[19] S.Usui, M.Kikuchi, *Journal of Non-Crystalline Solids* 34(1975) 1

[20] G.Lucovsky, C.Wang, M.J.Williams, Y.L.Chen, D.M.Maher, *Proc. Mat. Res. Soc. Symp.* 283 (1993) 443

[21] A. Matsuda,*J. Non-Cryst. Solids* 59 (1983) 767

[22] J. Meier, R. Fluckiger, H. Keppner, A. Shah *Appl. Phys. Lett.* 65 (1994) 860

[23] P. Torres, et al., *Appl. Phys. Lett.* 69 (1996) 1373

[24] Curtins et al, Plasma Chem Plasma Processing 7 (1987) 267

[25] Moisan et al, J. Vac. Sci. Technl 9(8) 1991

[26] D.L.Flamm, J. Vac. Sci. Technl 4(729) 1986

[27] A.A.Howling et al, J. Vac. Sci. Technl 10(4) 1992

[28] A.Gallagher, Int Journal of Solar energy, 5 (1988) 311

[29] A.Perret, P.Chabert, J.Jolly, J.P.Booth, *Appl. Phys. Lett.* 86 (2005) 021501

[30] J.L Dorier et al, J. Vac. Sci. Technl 10(1048) 1992

[31] S.Oda, J.Noda, *Jap. Journal of Applied Physics* 29 (1989) 1889

[32] C.L.Yang, Y.H.Shing, C.E Allevato,*Photovoltaic Specialists Conference, IEEE* (1988) 202

[33] A. Matsuda, J. Non-Cryst. Solids 59/60 (1983) 767.

[34] J. Perrin, M. Shiratani, P. Kae-Nune, H. Videlot, J. Jolly, J. Guillon, J. Vac. Sci. Technol. A 16 (1998) 278.

[35] A. Gallagher, J. Appl. Phys. 63 (1988) 2406

[36] S. Veprek, Z. Iqbal, F.A. Sarott, Phil. Mag. B 45 (1982) 137. C.C.

[37] Tsai, G.B. Anderson, R. Thompson, B. Wacker, J. Non-Cryst. Solids 114 (1989) 151.

[38] K. Nakamura, K. Yoshida, S. Takeoka, I. Shimizu, Jpn. J. Appl. Phys. 34 (1995) 442.

[39] S. Miyazaki, N. Fukuhara and M. Hirose, J. Non-Cryst. Solids 266 (2000), 59

[40] V.L. Dalal, Thin Solid Films 395 (2001) 173177

[41] A.Shah, et al., *Mat. Sci. and Eng.* 70 (2000) 219

[42] Hiroyuki Fujiwara, Michio Kondo, Akihisa Matsuda, *Physical Review B* 63 (2001) 115306

[43] A.Fejfar, T.Mates, O.Certik, B.Rezek, J.Stuchlik, I.Pelant, J.Kocka, *Journal of Non-Crystalline Solids* 5 (2004) 338

[44] J.Kocka et al., *Solar Energy Mater. And Solar cells* 78 (2003) 493

[45] W.E.Spear, P.G. LeComber, *Solid State Communication* 17(1975) 1193

[46] Arvind Shah et al., *Thin Solid Films* 403 2002 179

[47] C.Sal et al., *Thin Solid Films* 337 (1999) 152

[48] J.A.Tsai et al., *J. Electrochem. Soc* 142 (1995) 3220

[49] Takuya Matsui,Michio Kondo *Applied Physics Letters* 89 (2006) 142115

[50] S.krishnamrthy, A.Sher, A.Chen *Applied Physics Letters* 47 (1985) 160

[51] T.Matsui et al., *Journal of Non-Crystalline Solids* 352 (2006) 1255

[52] Hwaiyu Geng, Semiconductor Manufacturing Handbook, McGraw-Hill, 2005

[53] Adolf Goetzberger, Joachim Knobloch, Bernhard Voss,Crystalline Silicon Solar Cells, John Wiley, 1998

[54] S.Miyazaki, H.Takahashi, H.Yamashita, M.Narasaki, M.Hirose, *Journal of Non-Crystalline Solids* 299-302 (2002) 148-152

[55] L.Houben, R.Carius , D. Lundszien, J. Folsch , F.Finger, M.Luysberg and H.Wagner *Philosophical Magazoine Letters* 79 (1999) 71

[56] G.Ganguly, M.Fukawa, T.Ikeda, A.Matsuda, *Journal of Non-Crystalline Solids* 227-230 (1998) 1069-1073

[57] Xuejun Niu, Vikram Dalal, *Journal of Applied Physics* 98 (2005) 1

[58] M.Isomura et.al, *Solar energy materials and solar cells* 74 (2002) 519-524

[59] M.Isomura et.al, *Photovoltaic Specialists Conference, IEEE* 15-22 (2000) 776 - 779

[60] Jatindra K.Rath, F.D. Tichelaar, Ruud E.I Schropp, *Solar energy materials and solar cells* 74 (2002) 553-560

[61] D. Ritter, K. Weiser, and E. Zeldov, J. Appl. Phys. 62(1987) 4563

[62] A. M. Goodman,*Journal of Applied Physics* 32(1961)2250

[63] J. Kocka et.al, Mater. Res. Soc. Symp. Proc. 557(1999)483

[64] V. Svrcek et.al, *Journal of Applied Physics* 89, 1800 2001!.

[65] V. Svrcek, *Journal of Applied Physics* 92(2005)5

[66] V. A. Skidanov, M. S. Baev, and N. A. Baikova, Russian Microelectronics, Vol. 32, No. 2, 2003, pp. 9194

[67] R.A.Smith, Semiconductors, Cambridge University Press, 1959

[68] Ben G.Streetman, Sanjay Banerjee, Solid State Electronics, Fifth Edition, Prentice Hall of India, 2000

[69] S. Rein, T. Rehrl, W. Warta, S. W. Glunz,*Journal of Applied Physics* 91 (2002) 4

[70] T. Brammer and H. Stiebig, *Journal of Applied Physics* 94 (2003) 2

[71] Dieter K. Schroder, *IEEE Transactions On Electron Devices* 44 (1997) 1

[72] John F.O'Hanlon, A user's guide to vacuum technology, Thrid edition John Wiley & Sons Inc., 2003

[73] Wilbur C.Bigelow, Vacuum methods in electron microscopy, Vol.15, Portland Press, 1994

[74] Leon I.Maissel and Reinhard Glang, Handbook of thin film technology, McGraw-Hill, Inc., 1970

[75] Francis F.Chen and Jane P.Chang, Lecture notes on principles of plasma processing, Kluwer Academic, 2003

[76] M.A.Lieberman and A.J.Lichtenberg, Principles of plasma discharges and materials processing, John Wiley, 1994

[77] Mitsuharu Konuma, Plasma techniques for film despoitions, Alpha Science International Ltd,2005

[78] Colin N.Banwell and Elaine M.McCash, Fundamentals of molecular spectroscopy, Fourth edition, Tata McGraw-Hill, 1994

[79] B.D.Cullity and S.R.Stock, X-Ray Diffrraction, Thrid edition, Prentice Hall, 2001

[80] Puneet Sharma, Ph.D Thesis, Iowa State University (2005)

[81] O. Vetterl, M. Hlsbeck, J. Wolff, R. Carius and F. Finger *Thin Solid Films* 427 (2003) 46

[82] Kimerling.L. C., *Journal of Applied Physics* 45 (1974) 1839

[83] Daniel Stieler, Vikram L Dalal, Kamal Muthukrishnan, Max Noack and Eric Schares *Journal of Applied Physics* 100 (2006) 036106

[84] T.Dylla, S. Reynolds, R. Carius, F. Finger, *Journal of Non-Crystalline Solids* 352 (2006) 1093

[85] Benjamin Lax, S.F.Neustadter *Journal of Applied Physics* 25 (1954) 9

[86] Robert.H.Kingston *IRE Transactions on electron devices* 25 (1954) 829

[87] M.A.Melehey *IRE Transactions on electron devices* 25 (1961) 135

[88] Klaus Schunemann *IEEE Transactions on electron devices* 16(1976) 1151

[89] Hansjochen Benda, Eberhard Spenke *Proceedings of IEEE* 55 (1967) 8

[90] Andrew T.Yang,Yu Liu, T.Yao, R.R.Daniels *IEEE design automation conference* (1993) 720